https://doi.org/10.5194/acp-2020-1093
Preprint. Discussion started: 23 November 2020

Atmospheric Chemistry and Physics Discussions

Tropospheric and stratospheric wildfire smoke profiling with lidar: Mass, surface area, CCN and INP retrieval

Albert Ansmann[1], Kevin Ohneiser[1], Rodanthi-Elisavet Mamouri[2,3], Daniel A. Knopf[4], Igor Veselovskii[5], Holger Baars[1], Ronny Engelmann[1], Andreas Foth[6], Cristofer Jimenez[1], Patric Seifert[1], and Boris Barja[7]

[1]Leibniz Institute for Tropospheric Research, Leipzig, Germany
[2]Department of Civil Engineering and Geomatics, Cyprus University of Technology, Limassol, Cyprus
[3]ERATOSTHENES Center of Excellence, Limassol, Cyprus
[4]School of Marine and Atmospheric Sciences, Stony Brook University, Stony Brook, NY 11794-5000, USA
[5]Prokhorov General Physics Institute of the Russian Academy of Sciences, Moscow, Russia
[6]Leipzig Institute for Meteorology, University of Leipzig, Leipzig, Germany
[7]Atmospheric Research Laboratory, University of Magallanes, Punta Arenas, Chile

Correspondence: A. Ansmann
(albert@tropos.de)

Abstract. We present retrievals of tropospheric and stratospheric height profiles of particle mass, volume, and surface area concentrations in the case of wildfire smoke layers as well as estimates of smoke-related cloud condensation nucleus (CCN) and ice-nucleating particle (INP) concentrations from single-wavelength backscatter lidar measurements at ground and in space. A central role in the data analysis play conversion factors to convert the measured optical into microphysical properties. The set of needed conversion parameters for wildfire smoke are derived from AERONET observations of major smoke events caused by record-breaking wildfires in western Canada in August 2017 and southeastern Australia in January-February 2020. The new smoke analysis scheme is applied to stratospheric CALIPSO observations of fresh smoke plumes over northern Canada in 2017 and New Zealand in January 2020 and to ground-based lidar observation in southern Chile in aged Australian smoke layers in January 2020. These case studies show the potential of spaceborne and ground-based lidars to document large-scale and long-lasting wildfire smoke events in large detail and thus to provide valuable information for climate-, cloud-, and air chemistry modeling efforts performed to investigate the role of wildfire smoke in the atmospheric system.

1 Introduction

Record-breaking injections of Canadian and Australian wildfire smoke into the upper troposphere and lower stratosphere (UTLS) in 2017 and 2020 caused strong perturbations of stratospheric aerosol conditions in the northern and southern hemisphere. The smoke reached heights up to 23 km (Canadian smoke, 2017) (Hu et al., 2019; Baars et al., 2019; Torres et al., 2020) and more than 30 km (Australian smoke, 2020) (Ohneiser et al., 2020; Kablick et al., 2020; Khaykin et al., 2020), spread over large parts of the stratosphere, and remained detectable for 6-12 months. Smoke particles influence climate conditions by strong absorption of solar radiation, by acting as cloud condensation nuclei (CCN) and ice nucleating particles (INP) in cloud evolution processes (e.g., cirrus, polar stratospheric clouds), and by facilitating heterogeneous chemical processes due to the

https://doi.org/10.5194/acp-2020-1093
Preprint. Discussion started: 23 November 2020

Atmospheric Chemistry and Physics Discussions

significantly enhanced particle surface area concentration in the usually pristine stratosphere. Recent studies suggest that such major hemispheric perturbations may become more frequent in future within a changing global climate with more hot and dry weather conditions (Liu et al., 2009, 2014; Kitzberger et al., 2017; Jones et al., 2020).

Lidars around the world and in space are favorable instruments to monitor and document high altitude aerosol layers in the troposphere and lower stratosphere over long time periods. This was impressively demonstrated after major volcanic eruptions such as the El Chichon and Mt. Pinatubo events (Jäger, 2005; Trickl et al., 2013; Sakai et al., 2016; Zuev et al., 2019). As main aerosol proxies the directly observable particle backscatter coefficient and the related column-integrated backscatter are used. These optical quantities allow a precise and detailed study of the decay behavior of stratospheric aerosol perturbations. Furthermore, for volcanic aerosol a conversion technique was introduced to derive climate and air-chemistry-relevant parameters such as particle extinction coefficient and related aerosol optical thickness (AOT), mass, and surface area concentration from the backscatter lidar observations (Jäger and Hofmann, 1991; Jäger et al., 1995; Jäger and Deshler, 2002, 2003). Analogously, such a conversion scheme is needed for the analysis of free tropospheric and stratospheric wildfire smoke layers, but is not available yet. The two major stratospheric smoke events in 2017 and 2020 motivated us now to develop a respective smoke-related data analysis concept. The technique covers the retrieval of smoke microphysical properties and the estimation of cloud-relevant aerosol properties such as cloud condensation nucleus (CCN) and ice-nucleating particle (INP) number concentrations from single-wavelength lidar observations. A preliminary version of the new method was already applied to describe the decay of stratospheric perturbation after the major Canadian smoke injection in the second half year of 2017 (Baars et al., 2019). The retrieval scheme is easy to handle and applicable to lidar observation at the main lidar wavelengths of 355 and 532 nm and thus can also be used to evaluate measurements performed with the spaceborne CALIPSO (Cloud-Aerosol Lidar and Infrared Pathfinder Satellite Observation) lidar operated at 532 nm (Winker et al., 2009; Omar et al., 2009; Kar et al., 2019) and the 355 nm Aeolus lidar (Reitebuch, 2012; Reitebuch et al., 2020; Baars et al., 2020) which continuously monitor the global aerosol distribution.

For completeness, alternative lidar techniques are available to derive microphysical properties of smoke layers from lidar observations (Müller et al., 1999, 2014; Veselovskii et al., 2002, 2012). The so-called lidar inversion method was successfully applied to wildfire smoke layers in the troposphere (Wandinger et al., 2002; Murayama et al., 2004; Müller et al., 2005; Tesche et al., 2011; Alados-Arboledas et al., 2011; Veselovskii et al., 2015) as well as in the stratosphere (Haarig et al., 2018), and even to a stratospheric volcanic aerosol observation (Mattis et al., 2010). However, this sophisticated approach needs lidar observation at multiple wavelengths of very high quality and is strongly based on directly observed particle extinction coefficient profiles which are not easy to obtain especially not during the second and final phase of major stratospheric perturbations. The lidar inversion technique can sporadically provide valuable information about the relationship between the optical and microphysical properties of observed aerosol layers and thus can be used to check the reliability of applied AERONET-based POLIPHON conversion factors as shown in Sect. 4.2 and 4.3.

The article is organized as follows. An introduction into the complex chemical, microphysicaL, morphological, and optical properties of wildfire smoke and the ability of these particles to influence ice formation in clouds is given in Sect. 2. In Sect. 3, we provide an overview of the POLIPHON (Polarization lidar photometer networking) method (Mamouri and Ansmann,

https://doi.org/10.5194/acp-2020-1093
Preprint. Discussion started: 23 November 2020

Atmospheric Chemistry and Physics Discussions

2016, 2017) in which the new smoke retrieval method is integrated. The POLIPHON method basically combines polarization lidar and Aerosol Robotic Network (AERONET) (Holben et al., 1998) sunphotometer observations. A central role in the data analysis play conversion factors. The way how we determined these conversion factors is described in Sect. 3.4. Section 4 presents the set of conversion parameters for wildfire smoke as obtained from respective smoke observations with AERONET sunphotometers. Case studies of stratospheric smoke observations with the CALIPSO lidar over New Zealand in January 2020 and northern-central Canada in August 2017 and with a ground-based lidar in Punta Arenas, in southern Chile, in January 2020 are discussed in Sect. 5 to demonstrate the usefulness of the new smoke conversion technique. Concluding remarks are given in Sect. 6.

2 Wildfire smoke characteristics

The development of a smoke-related conversion method is a difficult task because of the complexity of smoke chemical, microphysical, and morphological properties. To facilitate the discussions in the next sections, a good knowledge of smoke characteristics is necessary and provided in this section. The overview is based on the smoke research and discussions presented by Fiebig et al. (2003); Müller et al. (2005, 2007); Dahlkötter et al. (2014); China et al. (2015, 2017); Knopf et al. (2018), and Liu and Mishchenko (2018, 2020).

2.1 Chemical, physical and morphological properties

First of all, the kind of fires, i.e., flaming versus smoldering combustion, the fuel type (burning material) and the combustion efficiency at given environmental conditions determine the initial chemical composition and size distribution of the smoke particles injected into the atmosphere. Burning of biomass at higher temperatures, during flaming fires, generates smaller particles than smoldering fires (Müller et al., 2005). In forest fires, the flaming stage is usually followed by a longer period of smoldering fires.

Smoke particles from forest fires are largely composed of organic material (organic carbon, OC) and, to a minor part, of black carbon (BC). The BC mass fraction is typically $<5\%$ (Dahlkötter et al., 2014). Biomass burning aerosol also consist of humic like substances (HULIS) which represent large macromolecules (Mayol-Bracero et al., 2002; Schmidl et al., 2008a, b; Fors et al., 2010; Graber and Rudich, 2006). The particles and released vapors within biomass burning plumes undergo chemical and physical aging processes during long-range transport. There is strong evidence from lidar observations that smoke particles grow in size during the aging phase (Müller et al., 2007). Processes that lead to the increase of particle size are hygroscopic growth of the particles, gas-to-particle conversion of inorganic and organic vapors during transport, condensation of large organic molecules from the gas phase in the first few hours of aging, coagulation, and photochemical and cloud-processing mechanisms. The lidar observations are in agreement with modeling studies of Fiebig et al. (2003) who used the theory of particle aging processes described by Reid and Hobbs (1998). Condensational growth dominates the increase of particle size in the first two days after emission of a plume. Thereafter coagulation in the increasingly diluted plumes becomes the dominating process. A significant shift of the particle size distribution indicated by an increase of the number median radius from about

https://doi.org/10.5194/acp-2020-1093
Preprint. Discussion started: 23 November 2020


Atmospheric Chemistry and Physics Discussions

0.2 μm shortly after emission to about 0.35 μm after six days of travel was found in several cases of Canadian smoke by Müller et al. (2007). The aging effect has to be considered in the retrieval of smoke conversion factors. We distinguish fresh, weakly aged, and aged smoke observations in Sect. 4.2.

Dahlkötter et al. (2014) analyzed aircraft in situ measurements of a smoke layer advected from North America and observed over Germany at 10-12 km height in September 2011 and found, in agreement with many other airborne in situ observations, an almost monomodal size distribution of smoke particles with a pronounced accumulation mode (particles with diameters from roughly 100 to 1000 nm) and a weak Aitken mode (particles with diameters $<$100 nm). A distinct coarse mode, i.e., a mode with particles with diameters $>$1000 nm, was absent. The size distribution is of key importance in the attempt to identify smoke layers and contrast them from mineral dust plumes (Haarig et al., 2018). This is reflected in the respective dust-vs-smoke conversion factors as discussed in Sect. 4. A strong pronounced coarse mode is characteristic for mineral dust.

The black-carbon-containing smoke particles showed coating thicknesses of roughly 50–220 nm and shell-to-core diameter ratios of typically 2-3. Dahlkötter et al. (2014) assumed a concentric-spheres core-shell morphology for the strongly light-absorbing BC core and further assumed purely light-scattering coating material (i.e., no absorption by the shell) in their analysis of the airborne in situ observations. The authors emphasized that their core-shell model is an idealized scenario because the BC cores of combustion particles are fractal-like or compact aggregates and BC can be mixed with light-scattering material in different ways, including, e.g., surface contact of BC with the light-scattering components, full immersion of BC in the light-scattering component or immersion of the light-scattering components in the BC aggregate. A process that can produce near-surface BC morphology is coagulation of almost bare BC aggregates with BC-free particles. Condensation of secondary organic or inorganic aerosol components on BC particles can either result in particles with core-shell morphology (concentric or eccentric) or with near-surface BC morphology. All these possible morphology features must be considered in the discussion and estimation of the smoke optical properties and of the potential of smoke particles to serve as INP (Sect. 3.3.2).

Changes in the morphology (size, shape, and internal structure) of smoke particles and their internal mixing state (e.g., soot particle coating) are ongoing during long-range transport. As China et al. (2015) pointed out, freshly emitted soot particles, i.e., BC particles, are typically hydrophobic, lacy fractal-like aggregates of carbonaceous monomers and become hydrophilic as a result of coating and other aging processes. Lace soot undergoes compaction upon humidification. All these effects lead to an increased ability of smoke particles to serve as CCN with increasing long-range travel time.

Soot compaction (and collapse of the core structures) changes also the scattering and absorption cross sections depending on the refractive index, the monomer diameter, and the structural details. Many publication dealing with the optical properties became available in recent years (China et al., 2015; Liu and Mishchenko, 2018, 2020; Kahnert, 2017; Yu et al., 2019; Gialitaki et al., 2020). Liu and Mishchenko (2018) mentioned that their model considers eleven different model morphologies ranging from bare soot to completely embedded soot–sulfate and soot–brown carbon mixtures. In agreement with earlier studies, they found that for the same amount of absorbing material, the absorption cross section of internally mixed soot can be more than twice that of bare soot. Thus absorption increases as soot accumulates more coating material during long-range transport. As a general finding of the modeling studies, the absorption enhancement is a complex function of many factors such as the size and shape of the soot aerosols, the mixing state, the location of soot within the host, and the amount and composition of the coating

https://doi.org/10.5194/acp-2020-1093
Preprint. Discussion started: 23 November 2020


Atmospheric Chemistry and Physics Discussions

material. All these facts make it necessary to distinguish between fresh smoke (1-2 days after injection), weakly or semi-aged smoke (3-5 days after release), and aged wildfire smoke (>5 days of long-range transport) in our attempt to determine smoke conversion parameters, as will be discussed in Sect. 4.

2.2 Cloud-relevant properties

As already mentioned, smoke particles after long-range transport seem to be favorable CCN because they become increasingly hydrophilic during aging. In contrast to the impact of smoke on cloud droplet formation, the characterization of their influence on ice nucleation is rather difficult. The link between ice nucleation efficiency and particle chemical and morphological properties and the ongoing modifications of the properties during long-range transport is largely unresolved (China et al., 2017). However, it is widely assumed that the ability of smoke particles to serve as INP mainly depends on the organic material (OM) in the shell of the coated smoke particles (Knopf et al., 2018). BC is not considered to be an important contributor to immersion freezing (Möhler et al., 2005; Ullrich et al., 2017; Schill et al., 2020; Kanji et al., 2020).

Knopf et al. (2018) present a review on the role of organic aerosol (OA) and OM in atmospheric ice nucleation. A unique feature of OA particles is that they can be amorphous and can exist in different phases, including liquid, semisolid, and solid (or glassy) states in response to changes in temperature (T) and relative humidity (RH) (Koop et al., 2011; Zobrist et al., 2008; Knopf et al., 2018). At low temperatures, e.g., in the UTLS region, where the atmospheric temperature can be as low as 180 K, it is conceivable to assume that the particles are in a glassy state. Most of the secondary organic aerosol particles are solid above 500 hPa (about 5 km) according to modeling studies and for temperatures <240 K (Shiraiwa et al., 2017).

It has been shown that humic and fulvic matter can act as deposition nucleation and immersion freezing INPs (Wang and Knopf, 2011; Rigg et al., 2013; Knopf and Alpert, 2013; Knopf et al., 2018). Furthemore, these macromolecules can undergo amorphous phase transition under typical tropospheric conditions (Wang et al., 2012; Slade et al., 2017) similar to the processes we assume the organic coating of the smoke particles experiences.

Aerosol particles serving as INPs usually provide an insoluble, solid surface that can facilitate the freezing of water (Knopf et al., 2018). Deposition ice nucleation is defined as ice formation occurring on the INP surface by water vapor deposition from the supersaturated gas phase. Though, recent studies suggest that deposition ice nucleation can be the result of pore condensation freezing, where homogeneous ice nucleation occurs at lower supersaturation in nanometer-sized pores (David et al., 2019; Marcolli, 2014). When the supercooled smoke particle takes up water or its shell deliquesces, immersion freezing can proceed, where the INP immersed in an aqueous solution can initiate freezing (Knopf et al., 2018; Berkemeier et al., 2014). Finally, if the smoke particle becomes completely liquid (and no insoluble part within the particle is left), homogeneous freezing will take place at temperatures below 235 K (Koop et al., 2000).

However, in reality, at given air mass lifting conditions, the ice nucleation process can be very complex. The time that solid OM needs for transition to a more liquid state, termed as humidity-induced amorphous deliquescence, can range from several minutes to days at temperatures low enough for ice formation (Mikhailov et al., 2009; Berkemeier et al., 2014; Knopf et al., 2018). Thus the phase change (as function of T and RH) can be longer than typical cloud activation time periods (governed by the updraft velocity), potentially inhibiting full deliquescence and allowing the OA or the organic coating to serve as INP.

https://doi.org/10.5194/acp-2020-1093
Preprint. Discussion started: 23 November 2020


Atmospheric Chemistry and Physics Discussions

When amorphous OA or OM are involved in ice nucleation, the condensed-phase diffusion processes within OA particles will most probably govern the ice nucleation pathway (Wang et al., 2012).

The following potential scenarios of atmospheric ice nucleation are uniquely attributable to the presence of amorphous OM: (1) Ice formation in the glassy region may be due to ice nucleation on the solid organic particle, i.e., deposition ice nucleation. (2) During partial deliquescence, a residual solid core is coated by an aqueous shell, and immersion freezing may proceed. (3) At full deliquescense RH, the particles are completely liquid (and contain no solid soot fragments), homogeneous freezing will occur at temperatures below about 238 K. (4) The presence of a glassy phase in disequilibrium with surrounding water vapor (e.g., cloud activation at fast updrafts as discussed below) may suppress or initiate ice nucleation beyond the homogeneous ice nucleation limit (Berkemeier et al., 2014; Knopf et al., 2018). A slower updraft velocity allows for more time for deliquescence to proceed, potentially resulting in full deliquescence of the OA particle at warmer and drier conditions compared to when a faster updraft is active. Therefore, the same OM can be present in different phase states under the same atmospheric thermodynamic conditions (i.e., T and relative humidity over ice RH_{i}), resulting in different ice nucleation pathways and corresponding ice nucleation rates. OA particle size or coating thickness can also impact the rate and atmospheric altitude of the organic phase change, as larger particles or thicker coatings require more time to reach full deliquescence (Charnawskas et al., 2017) . There are many more peculiarities of amorphous OM that makes INP parameterization and prediction efforts very complicated as discussed in detail by Knopf et al. (2018).

Since amorphous smoke OA may take up water and partially deliquesce resulting in an aqueous solution at possibly subsaturated conditions, we apply the water-activity based immersion freezing (ABIFM) parameterization (Knopf and Alpert, 2013; Alpert and Knopf, 2016) and homogeneous ice nucleation parameterization by Koop et al. (2000). ABIFM derives the number of INPs per volume of air for a given time period, when T, RH, and particle surface area s are known (see Sect. 3.3.3). A deposition ice nucleation scheme based on classical nucleation theory is outlined in addition (Sect. 3.3.5) to cover the potential pathway of glassy smoke particles to serve as INPs. Again, T, RH, and s are input in the INP estimation.

To demonstrate the prediction or retrieval of smoke INP profiles from lidar observations in Sect. 5, we apply exemplary two OA model systems serving as surrogates of amorphous organic smoke particles. One is based on a macromolecular humic or fulvic acid that undergoes amorphous phase transitions in response to changes in RH and T (Wang et al., 2012) and free troposphere long-range transported particles that possess an organic coating acting as INPs (China et al., 2017).

3 POLIPHON method: smoke retrieval

The POLIPHON method is described in detail by Mamouri and Ansmann (2016, 2017); Marinou et al. (2019); Ansmann et al. (2019a) and was introduced to analyze polarization lidar observations of aerosol profiles in a convenient and systematic way. The overall goal of the POLIPHON methodlogy is to provide the lidar community with a practical and compact retrieval package to derive environmental, climate- and cloud-relevant aerosol paramaters from basic backscatter coefficient profiles measured with polarization, Raman, high-spectral-resolution, multiwavelength or just wide-spread single-wavelength lidars disregarding whether they are operated at ground or in space.

https://doi.org/10.5194/acp-2020-1093
Preprint. Discussion started: 23 November 2020

Atmospheric Chemistry and Physics Discussions

The data analysis consists of four parts: In part A, dust and non-dust contributions to observed particle backscatter profiles are separated. This part includes further analysis (based on backward trajectories and, e.g., Raman lidar observations) to identify the non-dust aerosol type (marine aerosol or urban haze or biomass burning smoke). Examples of successful separation of biomass burning smoke and desert dust are presented by Tesche et al. (2009, 2011). In part B, the conversion of the aerosol-type-resolved backscatter coefficients into respective extinction coefficients and subsequently into microphyscial properties is performed. Part C deals with the estimation of cloud-relevant quantities (CCN and INP concentrations) for the identified aerosol types. Part D of the POLIPHON package covers the retrieval of the conversion parameters (required in part B) from photometer network (AERONET) observations. A detailed study of desert dust conversion factors was recently presented by Ansmann et al. (2019a). Now we present a similar approach for wildfire smoke.

The POLIPHON method is well validated in a variety of field activities (Mamali al., 2018; Düsing et al., 2018; Marinou et al., 2019; Haarig et al., 2019; Genz et al., 2011) and applied in numerous studies (Cordoba-Jabonero et al., 2018; Georgoulias et al., 2020; Marinou et al., 2019; Ansmann et al., 2019b; Baars et al., 2019; Costa-Surós et al., 2020; Hofer et al., 2020). In the following, we briefly summarize the different parts of the data analysis with special focus on wildfire smoke.

3.1 Part A: basic polarization lidar analysis

To keep the discussion short, we assume that the smoke layers were well detected and well identified, e.g., by means of air mass transport studies or, if available by spectrally resolved lidar observations of particle extinction-to-backscatter ratios (lidar ratios) and depolarization ratios (Haarig et al., 2018). To determine potential contributions of soil dust to particle backscattering in free-tropospheric smoke layers (Nisantzi et al., 2014; Wagner et al., 2018), the polarization lidar method can be used to determine and eliminate the dust fraction and to accurately quantify the smoke fraction (Tesche et al., 2009, 2011). Regarding stratospheric smoke layers, which are related to strong Pyro-Cb activity, we have no indication from polarization and lidar ratio observations for the presence of any soil dust traces in these high-altitude smoke layers (Haarig et al., 2018; Ohneiser et al., 2020). So we assume pure smoke layers when the smoke is detected in the stratosphere.

Figure 1 shows a stratospheric smoke layer observed with a polarization Raman lidar over Punta Arenas (53.2°S, 70.9°W), Chile, at the southernmost tip of South America (Ohneiser et al., 2020; Pollynet, 2020). The layer occurred between 20 and 26 km height on 29 January 2020. We will use this measurement as case study in Sect. 5 and will apply all conversion procedures to this observation.

3.2 Part B: Conversion into microphysical properties

Part B of the POLIPHON data analysis starts from the obtained aerosol-type-resolved backscatter coefficients. Since we exclusively focus on smoke and concentrate on the main lidar wavelength of 532 nm, we leave out to indicate laser wavelength and aerosol type as they were introduced in the original articles (Mamouri and Ansmann, 2016, 2017). An overview of all steps of the data analysis is provided in Table 1. In the case of smoke, the backscatter coefficients are converted to respective smoke extinction coefficients (step 2) by multiplication with an appropriate smoke lidar ratio S_{L}. Table 2 provides an overview of the large range of smoke lidar ratios. Extended overviews of smoke lidar ratios can be found in Haarig et al. (2018) and Nicolae

https://doi.org/10.5194/acp-2020-1093
Preprint. Discussion started: 23 November 2020

Atmospheric Chemistry and Physics Discussions

et al. (2013). The reason for the large spectrum of lidar ratios are the complex smoke properties (size, shape, composition) as discussed in Sect. 2.

We recommend to use a lidar ratio S_{L} of 45-55 sr for 355 nm and 65-80 sr for 532 nm if there is no possibility to obtain actual lidar ratio information from direct Raman lidar or High Spectral Resolution Lidar (HSRL) observations. For fresh smoke, an appropriate value for the lidar ratio seems to be 70-80 sr at both wavelength. Aged smoke shows a characteristic S_{L} ratio of $S_{\mathrm{L}}(355\ \mathrm{nm})/S_{\mathrm{L}}(532\ \mathrm{nm}) < 1$ which is not produced by any other aerosol type and allows a clear unambiguous identification of smoke layers (Müller et al., 2005; Noh et al., 2009; Nicolae et al., 2013; Ohneiser et al., 2020).

The smoke extinction coefficient is the basic parameter in the subsequent retrieval of volume, mass, surface area and number concentration and estimation of CCN and INP profiles. The smoke extinction coefficients are converted into volume concentrations $v(z)$ (step 3 in Table 1) by means of an appropriate smoke extinction-to-volume conversion factor c_{v}. To obtain the smoke mass concentration $M(z)$ (step 4), an estimate for the density ρ of the smoke particles is required. Li et al. (2016) investigated different smoke aerosols in the laboratory by burning of different straw types and found densities of 1.1 to 1.4 g cm^{-3} for the produced smoke particles. For organic particles ρ_{OM} was about 1.05±0.15 g cm^{-3} and for ρ_{EC} (elemental carbon) they yielded 1.8 g cm^{-3}. Chen et al. (2017) reviewed the smoke research in China and concluded that the smoke particle density is 1.0-1.9 g cm^{-3}. Thus in the cases with a few percent of BC the overall smoke particle density should be in the range of 1.0–1.3 g cm^{-3}.

Further POLIPHON conversion products are listed in Table 1 (steps 5-7). These are the surface area concentration s, two particle number concentrations n_{50} and n_{250} considering particles with radius >50 nm and >250 nm, respectively, and estimates of the CCN concentration n_{CCN} (assuming a water supersaturation value of S_{w} =0.2% during droplet nucleation) and the INP number concentration n_{INP}. The needed conversion factors c_{v}, c_{s}, c_{50}, c_{250}, and x (see Table 1) are obtained from AERONET observations during situations dominated by wildfire smoke. These results are presented in Sect. 4.

In Mamouri and Ansmann (2015, 2016), we explain how we calculate n_{250} and s from the downloaded AERONET size distribution data sets. The surface area concentration s and the large-particle concentration n_{250} are input parameters in INP retrievals (Knopf and Alpert, 2013; DeMott et al., 2015; Ullrich et al., 2017). The large-particle fraction with sizes (diameters) >500 nm can be regarded as the reservoir for favorable INPs.

Table 1 also provides an overview of typical uncertainties in the POLIPHON products (Mamouri and Ansmann, 2016, 2017). The very large uncertainties in the estimation of n_{50} and n_{CCN} are given when taking all potential error sources into consideration and are mostly related to the uncertainty in the conversion parameters. For n_{INP} we even do not provide uncertainty numbers which are probably in the range of a factor of 50 around the obtained INP solutions (Knopf and Alpert, 2013; China et al., 2017). As mentioned, more research is needed about the impact of smoke particles on ice nucleation before trustworthy uncertainty margins can be defined.

It should be emphasized in this context that the basic lidar-derived aerosol input parameters in the INP estimations s and n_{250} are available with a relative low uncertainty of 25-40%. And concerning the estimation of CCN concentrations, several direct comparison with in situ observations (Düsing et al., 2018; Haarig et al., 2019) show that the CCN retrieval uncertainty is typically less than a factor of 2.

https://doi.org/10.5194/acp-2020-1093
Preprint. Discussion started: 23 November 2020


Atmospheric Chemistry and Physics Discussions

3.3 Part C: Estimation of CCN and INP profiles

3.3.1 CCN

The CCN concentration is a strong function of updraft speed and thus water supersaturation S_{w}. The number concentration n_{50} roughly indicates the CCN concentration for weak updrafts and frequently observed low water supersaturations of $S_{\mathrm{w}} = 0.2\%$. Water supersaturation values may exceed even 1% in strong updrafts. Then the CCN concentrations may be a factor of >5 higher than n_{50}. For the conversion of σ into number concentration n_{50}, the conversion parameters c_{50} and exponent x as shown in Table 1 are used and obtained from the AERONET observations as discussed in Sects. 4.2.

In the original POLIPHON approach (Mamouri and Ansmann, 2016), we used n_{60} (particles with radius >60 nm) as a proxy for the CCN concentration (defined for dry aerosol particles) to account for ambient humidity conditions. It assumed that n_{60} represent the true number concentration (n_{50} for dry conditions) after drying the aerosol particles. However, the AERONET data analysis yield that practically no significant difference exist between n_{50} and n_{60} in the case of a pronounced smoke accumulation mode. So, n_{50} is a good proxy for smoke CCN concentration for typically weak supersaturations during cloud droplet nucleation.

3.3.2 INP

As discussed in Sect. 2.2, the estimation of INP concentrations is challenging due to the chemical complexity of the smoke aerosol. The parameterizations introduced in this section cover the OM-related ice nucleation for the temperature range in the upper troposphere ($< -40°$C). Only for these low temperatures, organic smoke particles may be able to influence ice nucleation in the atmosphere. In the following, we present procedures to compute INP concentrations for immersion freezing, deposition ice nucleation, and homogeneous freezing.

3.3.3 Immersion freezing parameterization

Organic smoke particles that have undergone long-range transport are chemically complex and INP paramterizations that capture the ice formation rate at upper tropospheric and lower stratospheric conditions (i.e., including subsaturated conditions) are scarce (Knopf et al., 2018). Knopf and Alpert (2013) introduced the water-activity-based immersion freezing model ABIFM, drawn from the water-activity-based homogeneous ice nucleation theory (Koop et al., 2000). Knopf and Alpert (2013) present an ABIFM parameterization for two types of humic compounds based also on experimental data by Rigg et al. (2013) that is valid for saturated and subsaturated atmospheric conditions. For demonstration of our method, we chose to apply the ABIFM for Leonardite (a standard humic acid surrogate material) to represent the amorphous organic coating of smoke particles. The ABIFM allows prediction of the ice particle production rate $J_{\mathrm{het,I}}$ as a function of ambient air temperature T (freezing temperature), ice supersaturation S_{i}, particle surface area s, and time period Δt for which a certain level of ice supersaturation S_{i} is given. For demonstration purposes, we simply assume a constant supersaturation period for 10 minutes (600 s). Such supersaturation conditions may occur during the upwind phase of a gravity wave.

https://doi.org/10.5194/acp-2020-1093
Preprint. Discussion started: 23 November 2020

Atmospheric Chemistry and Physics Discussions

According to Eqs. (6)-(8) in Alpert and Knopf (2016), we calulate the so-called water activity criterion (Koop et al., 2000) in the first step:

$$\Delta a_{\mathrm{w}} = a_{\mathrm{w}} - a_{\mathrm{w,i}}(T)\,. \tag{1}$$

The term $a_{\mathrm{w,i}}$ in Eq. (1),

$$a_{\mathrm{w,i}} = P_{\mathrm{i}}(T)/P_{\mathrm{w}}(T) \tag{2}$$

is the ratio of ice saturation pressure P_{i} to water saturation pressure P_{w} as function of temperature T and can be accurately determined by using Eq. (7) in Koop and Zobrist (2009). When condensed-phase and vapor phase are in equilibrium, the water activity a_{w} is equal to RH_{w} (written as 0.75 if RH_{w}=75%) in the air parcel in which ice nucleation takes place (e.g., in a cirrus layer at height z at temperature T). Relative humidity and temperature values may be available from radiosonde ascents or taken from data bases with re-analyzed global atmospheric data. However, the actual RH_{w} and T values during the lifting process (associated with cooling and increase in RH_{w} and decrease in T in the air parcel) remain always unknown and need to be estimated in the studies of a potential smoke impact on cirrus formation. The organic aerosol type Leonardite needs a relative humidity over ice RH_{i} of about 130% or $\Delta a_{\mathrm{w}} = 0.2$ at -50°C to become efficiently activated as INP.

In the next step, the ice crystal nucleation rate coefficient $J_{\mathrm{het,I}}$ (in cm^{-2} s^{-1}) is calculated:

$$\log_{10}(J_{\mathrm{het,I}}) = b + m\Delta a_{\mathrm{w}}\,. \tag{3}$$

The particle parameters b and m are determined from laboratory studies for different organic aerosol material. Table 3 contains the parameters for two different natural organic substances (Pahokee Peat and Leonardite) (Knopf and Alpert, 2013) which serve as surrogates of the organic coating of the atmospheric smoke particles. Leonardite, an oxidation product of lignite, is a humic-acid-containing soft waxy particle (mineraloid), black or brown in color, and soluble in alkaline solutions. Both substances served as surrogates for humic-like substances (HULIS, Sect. 2.1) in extended immersion freezing laboratory studies (Knopf and Alpert, 2013; Rigg et al., 2013). Organic aerosols containing HULIS are ubiquitous in the atmosphere. We also applied the ABIFM parameterization to aerosol samples representing free tropospheric aerosol (FTA, China et al., 2017) collected on substrates on the Azores for off-line micro-spectroscopic single-particle analysis and ice nucleation experiments. According to backward trajectories, the air masses arriving at the Azores crossed western parts of North America during the main fire season (August-September). FTA showed clear smoke signatures. Note that Eq. (3) delivers strongly fluctuating solutions of $J_{\mathrm{het,I}}$ when Δa_{w} is small, and robust, less fluctuating $J_{\mathrm{het,I}}$ values for $\Delta a_{\mathrm{w}} > 0.1$.

In the final step, we obtain the number concentration of smoke INP for the immersion freezing mode,

$$n_{\mathrm{INP,I}} = s J_{\mathrm{het,I}} \Delta t\,. \tag{4}$$

s is the surface area concentration of the smoke particles (Table 1, step 5) in cm^2 m^{-3} and Δt (in seconds) is the time period for which constant or almost constant ice supersaturation conditions are given. This can be the time period of a short updraft event (of a few minutes, 120-300 s) or of the lifting period of a gravity wave (>600 s). Long lasting lifting phases of gravity

https://doi.org/10.5194/acp-2020-1093
Preprint. Discussion started: 23 November 2020

Atmospheric Chemistry and Physics Discussions

waves can be up to 20 minutes (1200 seconds) as our Doppler lidar and radar observations conducted in several field campaigns during the last 10 years indicate.

3.3.4 Homogeneous freezing parameterization

Alternatively to smoke particles acting as heterogeneous INPs, we need to consider full deliquescence of smoke particles so that homogeneous freezing comes into play. Following Koop et al. (2000), the ice nucleation rate coefficient for homogeneous freezing is obtained from

$$\log_{10}(J_{\mathrm{hom}}) = -906.7 + 8502\Delta a_{\mathrm{w}} - 26924(\Delta a_{\mathrm{w}})^2 + 29180(\Delta a_{\mathrm{w}})^3 \tag{5}$$

for $0.26 < \Delta a_{\mathrm{w}} < 0.34$. The INP concentration is then obtained from

$$n_{\mathrm{INP,hom}} = v J_{\mathrm{hom}} \Delta t \tag{6}$$

with the particle volume concentration v (Table 1, step 3) in cm^3 m^{-3}. Homogeneous freezing proceeds at $RH_{\mathrm{i}} \approx 150\%$ at -50°C (i.e., $\Delta a_{\mathrm{w}} \approx 0.31$), whereas 130% ($\Delta a_{\mathrm{w}} = 0.2$) are required at -50°C to activate Leonardite-containing particles. Thus at slow ascend conditions heterogeneous ice nucleation on smoke particles may dominate ice formation in cirrus layers.

3.3.5 Deposition nucleation parameterization

Wang and Knopf (2011) provide a simplified parameterization of deposition ice nucleation (DIN) based on classical nucleation theory that describes the DIN efficiency of humic and fulvic acid compounds as a function of ambient temperature T and the humidity parameters RH_{i} and S_{i}. An alternative DIN parameterization is provided by, e.g., Hoose et al. (2010). A detailed description of the approach presented here is given in Sect. 3.6 in Wang and Knopf (2011) and thus only a brief introduction is given in the following.

The INP efficiencies are expressed as a function of the contact angle Θ which describes the relationship of surface free energies among the three involved interfaces including water vapor, ice embryo, and INP. Θ is parameterized as a function of RH_{i} (Eq. (8) in Wang and Knopf (2011)).

The compatibility parameter $m_{\Theta} = \cos(\Theta)$ (expressing the match between ice embryo and INP) is then used to determine the so-called geometric factor $f_{\mathrm{g}}(m_{\Theta})$ (Eq. (7) in Wang and Knopf (2011)), the free energy of ice embryo formation $\Delta F_{\mathrm{g,het}}(f_{\mathrm{g}}, T, S_{\mathrm{i}})$ (Eq. (6) in Wang and Knopf (2011)), and finally the ice crystal nucleation rate $J_{\mathrm{het,D}}$ (Eq. (5) in Wang and Knopf (2011)) in cm^{-2} s^{-1},

$$J_{\mathrm{het,D}} = 10^{25} \exp\left(\frac{\Delta F_{\mathrm{g,het}}}{k_{\mathrm{B}} T}\right) \tag{7}$$

with the Boltzmann constant k_{B}. The final step is then:

$$n_{\mathrm{INP,D}} = s J_{\mathrm{het,D}} \Delta t\,. \tag{8}$$

In terms of the contact-angle-based approach, $\Theta = 180°$ represents the case of homogeneous ice nucleation. The smaller Θ, the greater the propensity of the INP to act as deposition nucleation INP.

https://doi.org/10.5194/acp-2020-1093
Preprint. Discussion started: 23 November 2020

Atmospheric Chemistry and Physics Discussions

It remains to be emphasized again that the research on the smoke impact on atmospheric ice formation is ongoing (Knopf et al., 2018). Presently, uncertainties in the prediction of $J_{\mathrm{het,IF}}$ and $J_{\mathrm{het,DN}}$ for organic aerosols are very high (Wang and Knopf, 2011; China et al., 2017). However, the procedures introduced above allow us to estimate INP concentration profiles for organic aerosols and to study the potential impact of wildfire smoke on ice formation in tropospheric mixed-phase and ice clouds. Such smoke-cirrus investigations with lidar (and radar) may then trigger further laboratory work and will provide the means to better constrain INP parameterizations.

3.4 Part D: Smoke conversion parameters from sunphotometry

Part D of the POLIPHON method covers the AERONET data analysis part and deals with the determination of the smoke conversion parameters c_{v}, c_{s}, c_{50}, c_{250}, and the extinction wavelength exponent x (see Table 1). Trustworthy and climatologically robust conversion parameters are of central importance for the applicability and attractiveness of the POLIPHON method. The AERONET data base (AERONET, 2020) contains unique multiyear climatological data sets of spectrally resolved aerosol optical properties and related underlying microphysical properties of aerosol particles (e.g., size distribution, volume and surface area concentration) for a variety of different aerosol conditions, from purely marine, mineral dust, biomass burning smoke and anthropogenic haze events to situations with complex mixtures of these basic aerosol types. We used the advantage of the freely available AERONET data already to derive the conversion parameters for pure marine conditions (Mamouri and Ansmann, 2016, 2017) and pure desert dust scenarios (Ansmann et al., 2019a), and now continue with the determination of smoke conversion factors from smoke-dominated AERONET observations.

The smoke related study here is carried out for the main aerosol lidar wavelength of 532 nm. The AOT τ for 532 nm is obtained from the 440 nm AOT τ_{440} and the Ångström exponent a by

$$\tau = \tau_{440}(440/532)^{a}\,. \tag{9}$$

The Ångström exponent a (here for the 440 and 675 nm spectral range) is computed from the 440 and 675 nm AOTs, stored in the AERONET data base (AERONET, 2020).

To obtain, e.g., the extinction-to-volume conversion factor c_{v},

$$c_{\mathrm{v}} = \frac{V}{\tau}\,, \tag{10}$$

required to obtain volume and mass concentration from the lidar-derived particle extinction coefficients (see Table 1, steps 3 and 4), the ratio of the vertically integrated particle volume concentration V (denoted also as column volume concentration, available in the AERONET data base) and AOT τ is formed for each individual smoke observation.

Because the basic optical parameter in the lidar conversion procedures is the particle extinction coefficient σ (for smoke in this study), we introduce an arbitrary aerosol layer depth D and write

$$c_{\mathrm{v}} = \frac{V/D}{\tau/D} = \frac{v}{\sigma} \tag{11}$$

https://doi.org/10.5194/acp-2020-1093
Preprint. Discussion started: 23 November 2020

Atmospheric Chemistry and Physics Discussions

with the layer mean volume concentration v and the layer mean particle extinction coefficient σ. The introduced layer depth D has no impact on the further retrieval of the conversion factors and is only required to move from column-integrated values and AOT to more lidar-relevant quantities like concentrations and extinction coefficients.

For each smoke observation j (from number $j = 1$ to J), available in the AERONET data base for the selected smoke observational periods, we computed $c_{\mathrm{v},j}$ and then determine the mean value which we interpret as a representative smoke conversion factor,

$$c_{\mathrm{v}} = \frac{1}{J} \sum_{j=1}^{J} \frac{v_j}{\sigma_j} \,. \tag{12}$$

In the same way, the conversion factors c_{250}, needed to estimate the large-particle number concentration, and c_{s}, required in the surface-area retrieval, are computed:

$$c_{250} = \frac{1}{J} \sum_{j=1}^{J} \frac{n_{250,j}}{\sigma_j} \,, \tag{13}$$

$$c_{\mathrm{s}} = \frac{1}{J} \sum_{j=1}^{J} \frac{s_j}{\sigma_j} \,. \tag{14}$$

$$\tag{15}$$

In the retrieval of the conversion parameters required to obtain n_{50} (step 6 in Table 1), we used a different approach (Mamouri and Ansmann, 2016). Following the procedure suggested by Shinozuka et al. (2015), we applied a log-log regression analysis to the $\log(n_{50,j})$-$\log(\sigma_j)$ data field and determined in this way representative values for c_{50} and x that fulfill best the relationship,

$$\log\left(n_{50}\right) = \log\left(c_{50}\right) + x \log\left(\sigma\right) . \tag{16}$$

4 Smoke conversion parameters from the AERONET data base

We selected five AERONET stations for our in-depth wildfire-related AERONET data analysis. These stations and the used observational data sets (AOT, size distributions) are introduced in Sect. 4.1. The results of the AERONET data analysis are then discussed in Sect. 4.2 and summarized in Sect. 4.3.

Besides AERONET observations we include multiwavelength lidar observations of Australian smoke at Punta Arenas, southern Chile, and of Alaskan and Siberian smoke in the North Pole region in our study. Polly (*PO*rtab*L*le *L*idar s*Y*stem) instruments (Engelmann et al., 2016; Baars et al., 2016) were operated at Punta Arenas from November 2018 to the end of 2020 (Ohneiser et al., 2020) and aboard the German Research Vessel Polarstern in the North Pole region from September 2019 to September 2020. The Polly instruments permit the determination of height profiles of the particle backscatter coefficient at the laser wavelengths of 355, 532 and 1064 nm wavelength, particle extinction coefficients at 355 and 532 nm, and the particle linear depolarization ratio at 355 and 532 nm (Pollynet, 2020). From the backscatter and extinction coefficients, volume and surface

https://doi.org/10.5194/acp-2020-1093
Preprint. Discussion started: 23 November 2020


Atmospheric Chemistry and Physics Discussions

area concentrations, effective radius, and particle size distribution were derived and subsequently volume-to-extinction and surfarce-area-to-extinction conversion factors determined (Veselovskii et al., 2002, 2012).

We further include multiwavelength lidar observations of fresh and weakly aged smoke measured over the Amazon rainforest close to Manaus in September 2008 (Baars et al., 2012) and over the East coast of the United States close to Washington in August 2013 (Veselovskii et al., 2015) and of aged Canadian smoke measured over Leipzig in August 2017 (Haarig et al., 2018) and Lindenberg, 180 km northeast of Leipzig, Germany in August 1998 (Wandinger et al., 2002) and respectively derived conversion parameters of fresh and aged smoke in our study. The Lindenberg lidar observations documented for the first time that aged wildfire smoke can travel long distances over more than 10000 km without significant dissolution and removal (Forster et al., 2001).

Recently, large and optically dense tropospheric smoke plumes originating from major Californian wildfires crossed central Europe (11 and 12 September 2020). The highest, ever measured smoke-related tropospheric AOT (>0.5 at 500 nm) was recorded at the AERONET stations of Leipzig and Lindenberg in eastern Germany. We include this unique event in our study as well. The smoke plumes travelled rather fast, within three days, from California to central Europe.

4.1 AERONET sites, observational periods, smoke AOT and size distributions

The five selected AERONET stations are: Yellowknife (62.5°N, 114.4°W, 220 m height above sea level, a.s.l.) and Churchill (58.7°N, 93.8°W, and 10 m height a.s.l.) in northern Canada, CEILAP-RG (close to the city of Rio Gallegos, 51.6°S, 69.3°W, 19 m height a.s.l.) in southern Argentina, Punta Arenas (53.1°S, 70.9°W, 10 m height a.s.l.) in southern Chile, and Marambio (64.2°S, 56.6°W, 200 m a.s.l.) in the Argentine Antarctica. The measurements at Yellowknife and Churchill, shown in Fig. 2a, were performed 0.5–2.5 days and 2–5 days after the pyroCb-initiated injection of smoke in British Columbia, Canada, between 20:00 UTC on 12 August 2017 and 1:00 UTC on 13 August 2017, respectively. The smoke observations at CEILAP-RG, Punta Arenas and Marambio, presented in Fig. 2b, were taken about 10 days after injection in southeastern Australia (Ohneiser et al., 2020).

The AERONET sun/sky photometers allow the retrieval of the aerosol optical thickness (AOT) at eight wavelengths from 339 to 1638 nm (AERONET, 2020). Sky radiance observations at four wavelengths complete the AERONET observations. From these measurements the column–integrated particle size distribution, volume and surface area concentration, and number concentrations considering particles with radius >50 nm and >250 nm were derived.

As can be seen in Fig. 2a, fresh smoke arrived over Yellowknife, Canada, already 12-18 hours after injection. The 532 nm AOT reached values of almost 2.5. The smoke plumes travel southeastward and crossed Churchill about 1.5-4 days later. A maximum AOT of 2.7 was measured over Churchill. At clean background conditions the AOT is around 0.05 (dashed line in Fig. 2a) at the northern Canadian AERONET stations so that all AOTs >0.45 (solid line in Fig. 2a) used in our conversion study were clearly dominated by smoke light extinction. These data deliver conversion parameters for fresh (<2 days after injection) and weakly aged smoke (2-5 days after injection).

Figure 2b shows the observations of aged Australian wildfires smoke in southern South America and northern Antarctica. The smoke traveled more than 10000 km within 8-12 days. The diluted smoke caused 532 nm AOTs mostly between 0.2 and

https://doi.org/10.5194/acp-2020-1093
Preprint. Discussion started: 23 November 2020


Atmospheric Chemistry and Physics Discussions

0.3. Maximum values were close to 0.5-0.6. At clean background conditions, the AOT is in the range from 0.025–0.035. In our smoke-related AERONET data analysis we considered all observations with AOT>0.07 after careful checking that all used cases, even those with low AOT, showed clear and dominating smoke signatures. For each of the shown AOT observation we downloaded the microphysical quantities as well (AERONET, 2020). Figure 3 shows examples of size distributions of Australian wildfire smoke after long-range transport to South America and Antarctica. We included size distributions derived from multiwavelength lidar observations at Punta Arenas (Ohneiser et al., 2020) by using a lidar inversion method (Veselovskii et al., 2002, 2012).

In agreement with the discussion in Sect.2.1, a pronounced accumulation mode (centered at 200-350 nm radius) was observed. We noticed a weak coarse mode in part of the AERONET size distribution. This may be caused by injected Australian soil dust or by marine particles (in the lowest 500-1000 m of the troposphere) emitted by the southern Ocean. However, it cannot be excluded that the weak coarse mode is an artifact and a result of the AERONET retrieval procedure. The lidar-derived size distributions do not show a coarse mode in agreement with in situ observations in middle and upper tropospheric smoke plumes (Fiebig et al., 2003; Dahlkötter et al., 2014).

In Fig. 4, we compare different size distributions measured at the Canadian stations of Yellowknife and Churchill, and in Germany (Lindenberg close to Berlin) and southern Chile to highlight the expected growth of the smoke particles during long-range transport as discussed in Sect. 2.1. This aspect of particle growth and thus the contrast between fresh and aged smoke needs to be considered in the determination of the conversion factors. As can be seen, the smoke particles were smallest over Yellowknife (13 August, 23:18 UTC) 20 hours after injection. The particle size distribution then steadily shifted towards larger sizes with travel time (Churchill, 3.5 days, Punta Arenas 8 days, and Lindenberg 10.5 days after injection). All size distributions are normalized so that the integral over each shown size distribution is one. Lidar observation conducted at Leipzig, 180 km to the southwest of Lindenberg (Haarig et al., 2018) and over Punta Arenas agree qualitatively well with the respective AERONET size distributions.

In Fig. 5, we finally compare UTLS and stratospheric smoke size distributions derived from multiwavelength lidar observations over Leipzig (central Europe, Canadian smoke), Punta Arenas (southern South America, Australian smoke), and over the North Pole region (mostly Siberian and Alaskan wildfire smoke, 23 October and 7 Nov 2019). The aged smoke layers were detected between 15 and 16 km height over Leipzig, between 10 and 25 km over Punta Arenas, and from 8–17 km in the North Pole region. The smoke formed a persistent layer over the North Pole area for more than six months from autumn 2019 to late spring of 2020. All smoke size distributions show a pronounced accumulation mode.

4.2 AERONET observations: conversion parameters

Figure 6 (for aged smoke, January-February 2020) and 7 (for fresh and weakly aged smoke, August 2017) provide an overview of the relationship between the smoke volume concentration v and smoke extinction coefficient σ in (a), the particle surface area concentration s and σ in (b), and the particle number concentration of larger smoke particles n_{250} and σ in (c). For aged smoke, we distinguish between cases with monomodal (closed symbols) and bimodal size distribution (open symbols) in Fig. 6. The figures are based on 31 observations in southern hemisphere (Fig. 6) and 30 observations in the northern hemisphere (Fig 7).

https://doi.org/10.5194/acp-2020-1093
Preprint. Discussion started: 23 November 2020

Atmospheric Chemistry and Physics Discussions

We set the layer depth D in Eq. (11) arbitrarily to 1000 m so that σ (in Mm^{-1}) divided by 1000 yield the basic AERONET 532 nm AOT value. Several lidar inversion data sets (stars) for aged smoke (v vs σ and s vs σ) are included in Fig. 6. In Fig 7, we show the results of Fig. 6 again to highlight the differences between the correlations for fresh (including weakly aged) and aged smoke. Figure 8 finally focuses on fresh and weakly aged smoke and is based on a variety of lidar and AERONET observations (including the recent AERONET observations of tropospheric smoke in central Europe in September 2020).

As a general impression, a clear relationship between v, s, and n_{250} and σ is found for aged as well as for fresh smoke. The lidar observations agree well with the AERONET observations. We notice a small deviation between the correlation of volume concentration and extinction coefficient for monomodal and bimodal smoke size distributions in Figure. 6a. Such a clear difference is not visible in the correlation for the surface area concentration and large-particle number concentrations in Fig. 6b and c.

The mean conversion factors c_v (Eq. 12), c_s (Eq. 14), and c_{250} (Eq. 13) obtained from the AERONET observations are given as numbers in the different panels (in Fig. 6a for monomodal size distributions only). The respective link between v, s, and n_{250} and σ are visualized by straight lines. We did not distinguish between cases with monomodal and bimodal size distributions in Fig 7. All Yellowknife and Churchill size distributions showed a weak coarse mode.

The spread (or scatter) in the data provides an impression on the uncertainty in the conversion factors and mainly reflects variations in the smoke properties (size distribution, refractive index) but also to some extent in the AERONET retrieval uncertainties. The scatter in the Yellowknife and Churchill data in Fig 7 is larger because these AERONET observations cover the period with rapidly changing smoke properties of very fresh (Yellowknife) to weakly aged smoke plumes (Churchill).

Fig.7 corroborates that different conversion factors for fresh and aged smoke are needed. However, most smoke layers observed around the globe belong to the aged-smoke category. Nevertheless, spaceborne lidar allow a detailed view of the spread of smoke plumes from the first hours after injection to the end of the lifetime of the smoke events and thus need fresh smoke conversion factors to avoid systematic uncertainties in the decay behavior. Figure 8 indicates that a robust retrieval of volume and mass concentrations of fresh and weakly aged smoke is possible with one conversion data set, but that the surface area concentration, which is most directly linked to the measured optical properties, sensitively varies with slight changes in the particle size distribution so that the uncertainty in the surface area estimation is larger than in the volume estimation for fresh and weakly aged smoke.

Figure 9 shows the correlation between the CCN-relevant particle number concentration n_{50} and the extinction coefficient σ for both, fresh and aged smoke data sets. As recommended by Shinozuka et al. (2015) we correlated $\log(n_{50})$ vs $\log(\sigma)$. As outlined in Sect. 2, n_{50} (number concentration of dry particles with radius $>$50 nm) represents well the CCN reservoir for low water supersaturations of 0.2% (in the cloud base region where cloud droplet nucleation starts).

The conversion parameters were derived for dry stratospheric conditions. Liquid water clouds predominantly develop in the humid boundary layer and in the low part of the free troposphere. To account for moist ambient conditions in the CCN estimation, we may use a value 0.5σ (in the conversion, step 6 in Table 1) instead of the measured σ to correct roughly for water uptake effects which leads to an increase of σ by a factor of about 2 when the relative humidity increases from 40 to 80%.

https://doi.org/10.5194/acp-2020-1093
Preprint. Discussion started: 23 November 2020


Atmospheric Chemistry and Physics Discussions

All observations for fresh and aged smoke are given in Fig. 9 to better see the difference between aged and fresh smoke particle concentrations. According to the applied regression analysis, fresh smoke plumes contain much more CCN-relevant small particles (roughly a factor of 3 more) than aged plumes.

4.3 Overview of AERONET-derived conversion parameters

Table 4 summarizes the results of the AERONET study in the foregoing section and provides an overview of the derived conversion parameters. In the case of volume conversion factors for aged smoke, the factors derived for the monomodal size distribution are considered. For all other conversion parameters the entire AERONET data set as shown in Fig. 2 was used. Table 4 also includes conversion factors derived from the shown lidar observations. The lidar inversion results have a general uncertainty of 20-40%. The given SD values are calculated from 2-4 values available for each lidar profile and case.

Table 4 also contains a few values for the widely used mass-specific extinction coefficient k_{ext} at 532 nm, defined as $k_{\mathrm{ext}} = 1/(\rho c_{\mathrm{v}})$ (Ansmann et al., 2012). The range of k_{ext} values is computed for the smoke particle density ρ from 1.1–1.3 g m^{-3}. Aged smoke shows higher mass-specific extinction coefficients than fresh smoke.

At the end of the section it should be mentioned that the AERONET conversion parameters for 532 nm can be applied to 355 nm lidar observations if the wavelength dependence in the short wavelength range (355-532 nm), i.e., the ratio of σ_{355} to σ_{532} (index denotes weavelength in nm) is known. In case of multiwavelength lidars, the required wavelength dependence can be directly measured. The 355/532 nm extinction ratio was about 1.2 in the case of our North Pole observations, and around 1.2-1.5 for the Punta Arenas smoke observations.

5 Lidar case studies

We applied the new conversion scheme to ground-based (Polly, Punta Arenas) and spaceborne (CALIPSO) lidar observations to show how the data analysis works in practice. The cases demonstrate that backscatter lidars can significantly contributute to smoke profiling and smoke impact research.

5.1 Aged smoke over Punta Arenas

We start with the Polly measurement of Australian smoke at Punta Arenas shown in Fig. 1 (Pollynet, 2020). Figures 10–12 present the results of the conversions by following the procedure summarized in Table 1. In the first step, we calculated the extinction coefficients from the 532 nm backscatter coefficients by using an appropriate smoke lidar ratio of S_{L}=95 sr (Ohneiser et al., 2020) and then applied the AERONET-based conversion factor c_{v} in Table 4 for aged smoke to obtain the volume concentration (step 3 in Table 1). By assuming a particle density of 1.3 g cm^{-3} for the smoke particles, we obtain the mass concentration (step 4 in Table 1) shown in Fig. 10.

Such a high aerosol pollution level of 15 μg m^{-3} at heights from 20-26 km height has never been observed in the stratosphere before, even not after major volcanic eruptions (Trickl et al., 2013; Sakai et al., 2016). Stratospheric background levels are of the order of 0.01 μg m^{-3} (Baars et al., 2019; Taha et al., 2020).

https://doi.org/10.5194/acp-2020-1093
Preprint. Discussion started: 23 November 2020

Atmospheric Chemistry and Physics Discussions

Figure 11 shows the derived surface area concentration s and the particle number concentration n_{50}. The surface area concentration is an essential aerosol input parameter in the modeling of smoke-related heterogeneous chemical reactions in ozone depletion scenarios (Ansmann et al., 1996) and serves as input in the INP estimation shown in Figures 12. We present n_{50} profiles here to provide a full overview of the retrieval products, although such estimations are only relevant for heights where liquid-water clouds develop and thus for heights mainly below 5 km.

The INP estimation is the most crucial part of the data analysis as discussed in Sect. 2.2. We use the aerosol type parameters for Leonardite (LEO) and free tropospheric aerosol particles (FTA) as given in Table 3 in the estimation of immersion freezing INP ($n_{\mathrm{INP,I}}$, Sect. 3.3.3). The calculations start with the computation of the water activation criterion Δa_{w} (Eq. 1). Ice nucleation is a strong function of the vertical velocity (lifting of moist air parcels) which leads to ice supersaturation and thus determines Δa_{w}. In the case study here, we assume realistic upper-tropospheric cirrus formation conditions and ignore in this demonstration of INP number estimation that we observed the smoke layer in the dry stratosphere 10-15 km above the local tropopause. We assumed $RH_{\mathrm{w}} = 79.85\%$ and 82.35% and a temperature T of $-50°$C. The corresponding RH_{i} values are around 125% and 130%. Homogeneous freezing proceeds in significant numbers at about RH$_{\mathrm{i}}$ =150% at $-50°$C. Thus, for slow air lifting, smoke particles potentially acting as INPs have a good chance to sensitively influence cirrus formation. With these input values for RH_{w} and T, we obtain $\Delta a_{\mathrm{w}} = 0.175$ and 0.2. The value for the ice melting point $a_{\mathrm{w,i}}$ (Eq. 2) is 0.6235 at $-50°$C. Afterwards we calculated the ice nucleation rate $J_{\mathrm{het,I}}$ (Eq. 3) and the INP concentration $n_{\mathrm{INP,I}}$ (Eq. 4) by assuming a lifting period of 600 s during which ice supersaturation conditions according to Δa_{w} of 0.175 and 0.2 are given. We also computed deposition nucleation INP solutions ($n_{\mathrm{INP,D}}$, Sect. 3.3.5) by assuming the same T, RH_{i}, RH_{w}, and S_{i} input parameters together with an overall lifting period of 600 s.

Figure 12 shows the results of the $n_{\mathrm{INP,I}}$ and $n_{\mathrm{INP,D}}$ estimations. Obviously a threshold value of ice supersaturation S_{i} has to be reached and exceeded before efficient immersion freezing in the case of Leonardite starts. The estimated deposition nucleation INP concentration for Leonardite is much higher at $-50°$C and of the same order of magnitude as the INP concentration of immersion freezing in the case of FTA. The obtained high INP numbers are directly correlated to the large amount of smoke particles present and the assumed long activation time. These INP number concentrations are not too uncommon. For example, INP number concentrations reached about 10-100 L^{-1} in a Saharan dust plume (DeMott et al., 2003). Neglecting any radiative heating effects of the smoke layer and microphysical processes such as sedimentation and competition for water vapor, these results clearly indicate that organic smoke particles can impact ice formation processes in the upper troposphere during favorable moisture conditions and gravity wave activity.

In Fig. 12, also values for n_{250} (large particle fraction) are shown. It is usually assumed that particles with diameters $>$500 nm can be regarded as the overall reservoir for INPs (DeMott et al., 2015). Number concentrations of 10-100 cm^{-3} or 10000-100000 L^{-1} indicate that this reservoir of large smoke particles cannot be depleted when n_{INP} is in the range of 0.1 to 100 L^{-1}.

The competitive process to heterogeneous ice nucleation is homogeneous freezing. If ice supersaturation S_{i} reaches sufficient levels, corresponding to Δa_{w} of 0.29-0.31, $n_{\mathrm{INP,hom}}$ (Eq. 6) would be of the order of 600-700 L^{-1} for $v \approx 10^{-8}$ cm^3 L^{-1} (mean value of the 20-26 km layer).

https://doi.org/10.5194/acp-2020-1093
Preprint. Discussion started: 23 November 2020

Atmospheric Chemistry and Physics Discussions

As mentioned the uncertainty in the INP retrieval is large and is widely related to the current status of our knowledge about smoke INP type characteristics. The lidar input parameters s and v can be obtained with low uncertainty of 25-35%. The research on the role of wildfire smoke particles in cirrus and PSC formation is one of the key topics in atmospheric research with focus on aerosol-cloud interaction (Knopf et al., 2018).

5.2 Fresh smoke over Canada and New Zealand observed with CALIPSO lidar

We selected two CALIPSO lidar observations with smoke 1–3 days after injection to apply the fresh-smoke conversion factors in Table 4 (Yellowknife conversion parameters) (CALIPSO, 2020a, b). Figure 13 shows the smoke plume found over the northern part of New Zealand on 1 January 2020 injected via pyro-Cb events into the UTLS region over Southeast Australia on 30-31 December 2019 . The layer ascended by about 3 km during the first day of long-range travel by absorption of solar radiation by the smoke particles and heating of the surrounding air (Boers et al., 2010). Figure 14 presents the height profiles of smoke extinction coefficient, mass concentration, surface area concentration and estimated INP concentration (here for the water activity criterion of $\Delta a_{\mathrm{w}} = 0.2$ or RH_{i}=130% at $T = -50$°C, and $\Delta t = 600$ s). We used a lidar ratio of 95 sr to convert the measured smoke backscatter coefficients into extinction values. The stratospheric aerosol perturbation was roughly a factor of 10 higher in terms of extinction and mass concentration over New Zealand on 1 January 2020 than over Punta Arenas as observed with lidar on 9 January 2020, about 8 days later (not shown here) (Ohneiser et al., 2020). The background extinction level of a clean stratosphere is around 0.1 Mm^{-1} at 532 nm (Sakai et al., 2016; Baars et al., 2019; Taha et al., 2020). Again, INP concentrations were high enough to significantly influence cirrus formation.

Figure 15 finally shows a measurement of Canadian smoke observed with the CALIPSO lidar over the Hudson Bay, Canada, around 18:30 UTC on 15 August 2017, and thus almost 3 days (65 hours) after injection. In this case, strong pyro-Cb activity caused the smoke to ascent to about 10-11 km height over western Canada and then to further ascend by self-lifting effects up to 13-14 km height. The optical depth of the densest smoke plumes was rather high so that the lower boundary and the lower part of the smoke layer remained undetected. We therefore created a composite of different profile observations with smoke at lower and greater heights to obtain information about the smoke backscatter from 8 to 13 km height.

Figure 16 shows the derived height profiles of the smoke extinction coefficient, mass, surface area , and INP concentration. We used a lidar ratio of S_{L}=80 sr to transfer the backscatter into extinction coefficients and applied afterwards the smoke conversion parameters for fresh and weakly aged smoke in Table 4 (based Yellowknife and Churchill observations) to calculate v, M, and s. Again, a strong perturbation of the stratospheric aerosol conditions was found. High INP concentrations were derived, clearly indicating that smoke particles serving as INPs could significantly impact cirrus evolution at such high smoke pollution levels.

Figures 14 and 16 demonstrate that space lidars can provide much more information about detected smoke layers than height profiles of the basic lidar parameters (attenuated and particle backscatter). By conversion of the backscatter profiles into extinction coefficients, microphysical and cloud-relevant properties (INP concentrations) the modeling community dealing with the smoke impact on radiative transfer, cloud evolution, and heterogeneous chemical processes, can be significantly supported by spaceborne lidar observations providing data sets on a global scale.

https://doi.org/10.5194/acp-2020-1093
Preprint. Discussion started: 23 November 2020


Atmospheric Chemistry and Physics Discussions

6 Conclusion/Outlook

We presented a new method that permits the retrieval of tropospheric and stratospheric height profiles of smoke particle mass, volume, and surface area concentrations as well as first-order estimates of CCN and INP concentrations from single-wavelength backscatter lidar observations. The required conversion factors were determined from AERONET observations. In this approach, we distinguished fresh, weakly aged, and aged smoke observations. A crucial task is the estimation of smoke INP concentrations because of the complex characteristics of smoke particles. Now, a consistent methodology is available to characterize wildfire smoke plumes in terms of microphysical and cloud-relevant parameters. This will allow us to study smoke-cirrus interaction in large detail in future.

We applied the new smoke analysis scheme to ground-based as well as spaceborne CALIPSO observations to highlight the potential of single-wavelenth lidars (at ground and in space) to significantly contribute to an extended monitoring and microphysical characterization of tropospheric and stratospheric smoke layers and thus to provide valuable information for climate-, cloud-, and air chemistry modeling efforts.

7 Data availability

Polly lidar observations (level 0 data, measured signals) are in the PollyNET data base (Pollynet, 2020). LACROS observations (level 0 data) are stored in the Cloudnet data base (http://lacros.rsd.tropos.de). All the analysis products are available at TROPOS upon request (info@tropos.de). CALIPSO observations of smoke profiles and smoke AOT were used and downloaded from the CALIPSO data base (CALIPSO, 2020a, b)). AERONET observations were downloaded from the AERONET data base (AERONET, 2020).

8 Author contributions

The paper was written by AA with contributions (data analysis, methodological concepts) from KO, REM, DAK, IV, HB, and AF. The co-authors RE, CJ, PS, and BB were involved in the field observations and took care of all the smoke measurements with the Polly lidars at Punta Arenas and aboard RV Polarstern.

9 Competing interests

The authors declare that they have no conflict of interest.

10 Financial support

The authors acknowledge support through the European Research Infrastructure for the observation of Aerosol, Clouds and Trace Gases ACTRIS under grant agreement no. 654109 and 739530 from the European Union's Horizon 2020 research and

https://doi.org/10.5194/acp-2020-1093
Preprint. Discussion started: 23 November 2020

innovation programme. We thank AERONET-Europe for providing an excellent calibration service. AERONET-Europe is part of the ACTRIS project. R.-E. M. has been financial supported by the SIROCCO project (grant no. EXCELLENCE/1216/0217) co-funded by the Republic of Cyprus and the structural funds of the European Union for Cyprus through the Research and Innovation Foundation. Thanks are also provided to the ERATOSTHENES Centre of Excellence which was established after receiving funding by the Republic of Cyprus and the EU H2020 Widespread Teaming program with Grant Agreement No 857510 (www.excelsior2020.eu). The field observations at Punta Arenas are partly funded by the German Science Foundation (DFG) project PICNICC with project number 408008112. The development of the lidar inversion algorithm used to analyze Polly data was supported by the Russian Science Foundation (project 16-17-10241). D.K. acknowledges support by the DOE grant DE-SC0021034. The Polarstern Polly data was produced as part of the international Multidisciplinary drifting Observatory for the Study of the Arctic Climate (MOSAiC) with the tag MOSAiC20192020 and Project ID AWI_PS122_00.

The publication of this article was funded by the Open Access Fund of the Leibniz Association

Acknowledgements. We thank AERONET for their continuous efforts in providing high-quality measurements and products. We are grateful to the AERONET site managers Jacobo Salvador, Raul D'Elia, Ramiro Gonzales, and Jonathan Ferrarae (Ceilap-RG, Marambio), Norman O'Neill, Ihab Abboud, and Vitali Fioletov (Yellowknife, Chuchill), and Ralf Becker (Lindenberg). We also thank the CALIPSO team for their well-organized easy-to-use internet platforms. We are grateful to the MOSAiC and RV Polarstern teams for perfect logistical support.

https://doi.org/10.5194/acp-2020-1093
Preprint. Discussion started: 23 November 2020

Atmospheric Chemistry and Physics Discussions

References

AERONET: Aerosol Robotic Network aerosol data base, available at: http://aeronet.gsfc.nasa.gov/, last access: 20 August, 2020.

Alados-Arboledas, L., Müller, D, Guerrero-Rascado, J. L., Navas-Guzmán, F., Pérez-Ramírez, D., and Olmo, F. J.: Optical and microphysical properties of fresh biomass burning aerosol retrieved by Raman lidar, and star- and sun-photometry, Geophys. Res. Lett., 38, L01807, doi:10.1029/2010GL045999, 2011.

Alpert, P. A. and Knopf, D. A.: Analysis of isothermal and cooling-rate-dependent immersion freezing by a unifying stochastic ice nucleation model, Atmos. Chem. Phys., 16, 2083–2107, https://doi.org/10.5194/acp-16-2083-2016, 2016.

Ansmann, A., Wagner, F., Wandinger, U., Mattis, I., Görsdorf, U., Dier, H.-D., and Reichardt, J.: Pinatubo aerosol and stratospheric ozone reduction: Observations over central Europe, J. Geophys. Res., 101(D13), 18775– 18785, doi:10.1029/96JD01373, 1996

Ansmann, A., Seifert, P., Tesche, M., and Wandinger, U.: Profiling of fine and coarse particle mass: case studies of Saharan dust and Eyjafjallajökull/Grimsvötn volcanic plumes, Atmos. Chem. Phys., 12, 9399-9415, doi:10.5194/acp-12-9399-2012, 2012.

Ansmann, A., Baars, H., Chudnovsky, A., Mattis, I., Veselovskii, I., Haarig, M., Seifert, P., Engelmann, R., and Wandinger, U.: Extreme levels of Canadian wildfire smoke in the stratosphere over central Europe on 21–22 August 2017, Atmos. Chem. Phys., 18, 11831-11845, https://doi.org/10.5194/acp-18-11831-2018, 2018.

Ansmann, A., Mamouri, R.-E., Hofer, J., Baars, H., Althausen, D., and Abdullaev, S. F.: Dust mass, cloud condensation nuclei, and ice-nucleating particle profiling with polarization lidar: updated POLIPHON conversion factors from global AERONET analysis, Atmos. Meas. Tech., 12, 4849–4865, https://doi.org/10.5194/amt-12-4849-2019, 2019a.

Ansmann, A., Mamouri, R.-E., Bühl, J., Seifert, P., Engelmann, R., Hofer, J., Nisantzi, A., Atkinson, J., Kanji, Z., Amiridis, V., Vrekoussis, M., and Sciare, J.: Closure between ice-nucleating particle and ice crystal number concentration: Active remote sensing of altocumulus and cirrus clouds in Saharan dust over Cyprus, Atmos. Chem. Phys., in preparation, 2019b.

Australian Bureau of Meteorology: http://www.bom.gov.au/climate/current/annual/aus/

Baars, H., Ansmann, A., Althausen, D., Engelmann, R., Heese, B., Müller, D., Artaxo, P., Paixao, M., Pauliquevis, T., and Souza, R.: Aerosol profiling with lidar in the Amazon Basin during the wet and dry season, J. Geophys. Res., 117, D21201, doi:10.1029/2012JD018338, 2012.

Baars, H., Kanitz, T., Engelmann, R., Althausen, D., Heese, B., Komppula, M., Preißler, J., Tesche, M., Ansmann, A., Wandinger, U., Lim, J.-H., Ahn, J. Y., Stachlewska, I. S., Amiridis, V., Marinou, E., Seifert, P., Hofer, J., Skupin, A., Schneider, F., Bohlmann, S., Foth, A., Bley, S., Pfüller, A., Giannakaki, E., Lihavainen, H., Viisanen, Y., Hooda, R. K., Pereira, S. N., Bortoli, D., Wagner, F., Mattis, I., Janicka, L., Markowicz, K. M., Achtert, P., Artaxo, P., Pauliquevis, T., Souza, R. A. F., Sharma, V. P., van Zyl, P. G., Beukes, J. P., Sun, J., Rohwer, E. G., Deng, R., Mamouri, R.-E., and Zamorano, F.: An overview of the first decade of PollyNET: an emerging network of automated Raman-polarization lidars for continuous aerosol profiling, Atmos. Chem. Phys., 16, 5111-5137, https://doi.org/10.5194/acp-16-5111-2016, 2016.

Baars, H., Ansmann, A., Ohneiser, K., Haarig, M., Engelmann, R., Althausen, D., Hanssen, I., Gausa, M., Pietruczuk, A., Szkop, A., Stachlewska, I. S., Wang, D., Reichardt, J., Skupin, A., Mattis, I., Trickl, T., Vogelmann, H., Navas-Guzmán, F., Haefele, A., Acheson, K., Ruth, A. A., Tatarov, B., Müller, D., Hu, Q., Podvin, T., Goloub, P., Veselovskii, I., Pietras, C., Haeffelin, M., Fréville, P., Sicard, M., Comerón, A., Fernández García, A. J., Molero Menéndez, F., Córdoba-Jabonero, C., Guerrero-Rascado, J. L., Alados-Arboledas, L., Bortoli, D., Costa, M. J., Dionisi, D., Liberti, G. L., Wang, X., Sannino, A., Papagiannopoulos, N., Boselli, A., Mona, L., D'Amico, G., Romano, S., Perrone, M. R., Belegante, L., Nicolae, D., Grigorov, I., Gialitaki, A., Amiridis, V., Soupiona, O., Papayannis, A.,

Mamouri, R.-E., Nisantzi, A., Heese, B., Hofer, J., Schechner, Y. Y., Wandinger, U., and Pappalardo, G.: The unprecedented 2017–2018 stratospheric smoke event: decay phase and aerosol properties observed with the EARLINET, Atmos. Chem. Phys., 19, 15183–15198, https://doi.org/10.5194/acp-19-15183-2019, 2019.

Baars, H., Geiß, A., Wandinger, U., Herzog, A., Engelmann, R.,Bühl, J., Radenz, M., Seifert, P., Althausen, D., Heese, B., Ansmann, A., Martin, A., Leinweber, R., Lehmann, V., Weissmann,M., Cress, A., Filioglou, M., Komppula, M., and Reitebuch, O.: First results from the German Cal/Val activities for Aeolus, EPJ Web of Conferences, Volume 237, 01008, The 29th International Laser Radar Conference (ILRC 29), 24–28 June 2019, Hefei, Anhui, China, https://doi.org/10.1051/epjconf/202023701008, 2020.

Berkemeier, T., Shiraiwa, M., Pöschl, U., and Koop, T.: Competition between water uptake and ice nucleation by glassy organic aerosol particles, Atmos. Chem. Phys., 14, 12513–12531, https://doi.org/10.5194/acp-14-12513-2014, 2014.

Boers, R., de Laat, A. T., Stein Zweers, D. C., and Dirksen, R. J.: Lifting potential of solar-heated aerosol layers, Geophys. Res. Lett., 37, L24802, doi:10.1029/2010GL045171, 2010.

CALIPSO: Cloud–Aerosol Lidar and Infrared Pathfinder Satellite Observation Lidar Level 2 data, height-time displays of attenuated backscatter, available at https://www-calipso.larc.nasa.gov/products/lidar/browse_images/std_v4_index.php, last access: 20 August, 2020a.

CALIPSO: Cloud–Aerosol Lidar and Infrared Pathfinder Satellite Observation Lidar Level 2 data, particle backscatter profiles, available at https://search.earthdata.nasa.gov/search?fp=CALIPSO&fi=CALIOP, last access: 20 August, 2020b.

Charnawskas, J. C., Alpert, P. A., Lambe,, A. T., Berkemeier, T., O'Brien, R. E., Massoli, P., Onasch, T. B., Shiraiwa, M., Moffet, R. C., Gilles, M. K., Davidovits, P., Worsnop, D. R., and Knopf, D. A., Condensed-phase biogenic-anthropogenic interactions with implications for cold cloud formation, Farad. Discuss., 200, 165-194, doi: 10.1039/c7fd00010c, 2017.

Chen, J., Li, C, Ristovski, Z., Milic, A., Gu, Y., Islam, M. S., Wang, S., Hao, J., Zhang, H., He, C., Guo, H., Fu, H., Miljevic, B., Morawska, L., Thai, P., Lam, Y. F., Pereira, G., Ding, A., Huang, X., and Dumka, U. C., A review of biomass burning: Emissions and impacts on air quality, health and climate in China, Sci Total Environ., 579, 1000–1034, doi:10.1016/j.scitotenv.2016.11.025, 2017.

China, S., Scarnato, B., Owen, R. C., Zhang, B., Ampadu, M. T., Kumar, S., Dzepina, K., Dziobak, M. P., Fialho, P., Perlinger, J. A., Hueber, J., Helmig, D., Mazzoleni, L. R., and Mazzoleni, C.: Morphology and mixing state of aged soot particles at a remote marine free troposphere site: Implications for optical properties, Geophys. Res. Lett., 42, 1243–1250, doi: 10.1002/2014GL062404, 2015.

China, S., Alpert, P. A., Zhang, B., Schum, S., Dzepina, K., Wright, K., Owen, R. C., Fialho, P., Mazzoleni, L. R., Mazzoleni, C., and Knopf, D. A.: Ice cloud formation potential by free tropospheric particles from long-range transport over the Northern Atlantic Ocean, J. Geophys. Res. Atmos., 122, 3065– 3079, doi:10.1002/2016JD025817, 2017.

Cordoba-Jabonero, C., Sicard, M., Ansmann, A., del Aguila, A., and Baars, H.: Separation of the optical and mass features of particle components in different aerosol mixtures by using POLIPHON retrievals in synergy with continuous polarized Micro-Pulse Lidar (P-MPL) measurements, Atmos. Meas. Tech., 11, 4775-4795, https://doi.org/10.5194/amt-11-4775-2018, 2018.

Costa-Surós, M., Sourdeval, O., Acquistapace, C., Baars, H., Carbajal Henken, C., Genz, C., Hesemann, J., Jimenez, C., König, M., Kretzschmar, J., Madenach, N., Meyer, C. I., Schrödner, R., Seifert, P., Senf, F., Brueck, M., Cioni, G., Engels, J. F., Fieg, K., Gorges, K., Heinze, R., Siligam, P. K., Burkhardt, U., Crewell, S., Hoose, C., Seifert, A., Tegen, I., and Quaas, J.: Detection and attribution of aerosol-cloud interactions in large-domain large-eddy simulations with the ICOsahedral Non-hydrostatic model, Atmos. Chem. Phys., 20, 5657–5678, https://doi.org/10.5194/acp-20-5657-2020, 2020.

https://doi.org/10.5194/acp-2020-1093
Preprint. Discussion started: 23 November 2020

Dahlkötter, F., Gysel, M., Sauer, D., Minikin, A., Baumann, R., Seifert, P., Ansmann, A., Fromm, M., Voigt, C., and Weinzierl, B.: The Pagami Creek smoke plume after long-range transport to the upper troposphere over Europe – aerosol properties and black carbon mixing state, Atmos. Chem. Phys., 14, 6111–6137, https://doi.org/10.5194/acp-14-6111-2014, 2014.

David, R. O., Marcolli, C., Fahrni, J., Qiu, Y., Perez Sirkin, Y. A., Molinero, V., Mahrt, F., Brühwiler, D., Lohmann, U., and Kanji, Z. A.: Pore condensation and freezing is responsible for ice formation below water saturation for porous particles, Proc. National Academy of Sciences, 116, 8184-8189, doi:10.1073/pnas.1813647116, 2019.

DeMott, P. J., Sassen, K., Poellot, M. R., Baumgardner, D., Rogers, D. C., Brooks, S. D., Prenni, A. J., and Kreidenweis, S. M.: African dust aerosols as atmospheric ice nuclei, Geophys. Res. Lett., 30, 1732, doi:10.1029/2003GL017410, 2003.

DeMott, P. J., Prenni, A. J., McMeeking, G. R., Sullivan, R. C., Petters, M. D., Tobo, Y., Niemand, M., Möhler, O., Snider, J. R., Wang, Z., and Kreidenweis, S. M.: Integrating laboratory and field data to quantify the immersion freezing ice nucleation activity of mineral dust particles, Atmos. Chem. Phys., 15, 393–409, doi:10.5194/acp-15-393-2015, 2015.

Düsing, S., Wehner, B., Seifert, P., Ansmann, A., Baars, H., Ditas, F., Henning, S., Ma, N., Poulain, L., Siebert, H., Wiedensohler, A., and Macke, A.: Helicopter-borne observations of the continental background aerosol in combination with remote sensing and ground-based measurements, Atmos. Chem. Phys., 18, 1263-1290, https://doi.org/10.5194/acp-18-1263-2018, 2018.

Engelmann, R., Kanitz, T., Baars, H., Heese, B., Althausen, D., Skupin, A., Wandinger, U., Komppula, M., Stachlewska, I. S., Amiridis, V., Marinou, E., Mattis, I., Linné, H., and Ansmann, A.: The automated multiwavelength Raman polarization and water-vapor lidar PollyXT: the neXT generation, Atmos. Meas. Tech., 9, 1767-1784, doi:10.5194/amt-9-1767-2016, 2016.

Fiebig, M., Stohl, A., Wendisch, M., Eckhardt, S., and Petzold, A.: Dependence of solar radiative forcing of forest fire aerosol on aging and state of mixture, Atmos. Chem. Phys., 3, 881–891, https://doi.org/10.5194/acp-3-881-2003, 2003.

Fors, E. O., Rissler, J., Massling, A., Svenningsson, B., Andreae, M. O., Dusek, U., Frank, G. P., Hoffer, A., Bilde, M., Kiss, G., Janitsek, S., Henning, S., Facchini, M. C., Decesari, S., and Swietlicki, E.: Hygroscopic properties of Amazonian biomass burning and European background HULIS and investigation of their effects on surface tension with two models linking H-TDMA to CCNC data, Atmos. Chem. Phys., 10, 5625–5639, https://doi.org/10.5194/acp-10-5625-2010, 2010.

Forster, C., Wandinger, U., Wotawa, G., James, P., Mattis, I., Al-thausen, D., Simmonds, P., O'Doherty, S., Jennings, S., Kleefeld,C., Schnieder, J., Trickl, T., Kreipl, S., Jäger, H., and Stohl, A.: Transport of boreal forest fire emissions from Canada to Europe, J. Geophys. Res., 106, 22887–22906, 2001.

Genz, C., Schrödner, R., Heinold, B., Henning, S., Baars, H., Spindler, G., and Tegen, I.: Estimation of cloud condensation nuclei number concentrations and comparison to in situ and lidar observations during the HOPE experiments, Atmos. Chem. Phys., 20, 8787–8806, https://doi.org/10.5194/acp-20-8787-2020, 2020.

Georgoulias, A. K., Marinou, E., Tsekeri, A., Proestakis, E., Akritidis, D., Alexandri, G., Zanis, P., Balis, D., Marenco, F., Tesche, M., and Amiridis, V.: A first case study of CCN concentrations from spaceborne lidar observations, Remote Sens.,12, 1557, https://doi.org/10.3390/rs12101557, 2020.

Gialitaki, A., Tsekeri, A., Amiridis, V., Ceolato, R., Paulien, L., Kampouri, A., Gkikas, A., Solomos, S., Marinou, E., Haarig, M., Baars, H., Ansmann, A., Lapyonok, T., Lopatin, A., Dubovik, O., Groß, S., Wirth, M., Tsichla, M., Tsikoudi, I., and Balis, D.: Is the near-spherical shape the "new black" for smoke?, Atmos. Chem. Phys., 20, 14005–14021, https://doi.org/10.5194/acp-20-14005-2020, 2020.

Giannakaki, E., Pfüller, A., Korhonen, K., Mielonen, T., Laakso, L., Vakkari, V., Baars, H., Engelmann, R., Beukes, J. P., Van Zyl, P. G., Josipovic, M., Tiitta, P., Chiloane, K., Piketh, S., Lihavainen, H., Lehtinen, K. E. J., and Komppula, M.: One year of Raman lidar

observations of free-tropospheric aerosol layers over South Africa, Atmos. Chem. Phys., 15, 5429–5442, doi:10.5194/acp15-5429-2015, 2015.

Graber, E. R. and Rudich, Y.: Atmospheric HULIS: How humic-like are they? A comprehensive and critical review, Atmos. Chem. Phys., 6, 729–753, https://doi.org/10.5194/acp-6-729-2006, 2006.

Haarig, M., Ansmann, A., Baars, H., Jimenez, C., Veselovskii, I., Engelmann, R., and Althausen, D.: Depolarization and lidar ratios at 355, 532, and 1064 nm and microphysical properties of aged tropospheric and stratospheric Canadian wildfire smoke, Atmos. Chem. Phys., 18, 11847-11861, https://doi.org/10.5194/acp-18-11847-2018, 2018.

Haarig, M., Walser, A., Ansmann, A., Dollner, M., Althausen, D., Sauer, D., Farrell, D., and Weinzierl, B.: CCN concentration and INP-relevant aerosol profiles in the Saharan Air Layer over Barbados from polarization lidar and airborne in situ measurements, Atmos. Chem. Phys. Discuss., https://doi.org/10.5194/acp-2019-466, in review, 2019.

Hofer, J., Ansmann, A., Althausen, D., Engelmann, R., Baars, H., Abdullaev, S. F., and Makhmudov, A. N.: Long-term profiling of aerosol light extinction, particle mass, cloud condensation nuclei, and ice-nucleating particle concentration over Dushanbe, Tajikistan, in Central Asia, Atmos. Chem. Phys., 20, 4695–4711, https://doi.org/10.5194/acp-20-4695-2020, 2020.

Holben, B. N., Eck, T. F., Slutsker, I., Tanré, D., Buis, J. P., Setzer, A., Vermote, E., Reagan, J. A., Kaufman, Y. J., Nakajima, T., Lavenu, F., Jankowiak, I., and Smirnov, A.: AERONET – a federated instrument network and data archive for aerosol characterization, Remote Sens. Environ., 66, 1–16, 1998.

Hoose, C., Kristjánsson,J. E., Chen, J., and Hazra, A.: A classical-theory-based parameterization of heterogeneous ice nucleation by mineral dust, soot, and biological particles in a global climate model. J. Atmos. Sci., 67, 2483–2503, https://doi.org/10.1175/2010JAS3425.1., 2010.

Hu, Q., Goloub, P., Veselovskii, I., Bravo-Aranda, J.-A., Popovici, I. E., Podvin, T., Haeffelin, M., Lopatin, A., Dubovik, O., Pietras, C., Huang, X., Torres, B., and Chen, C.: Long-range-transported Canadian smoke plumes in the lower stratosphere over northern France, Atmos. Chem. Phys., 19, 1173-1193, https://doi.org/10.5194/acp-19-1173-2019, 2019.

Jäger, H.: Long-term record of lidar observations of the stratospheric aerosol layer at Garmisch-Partenkirchen, J. Geophys.Res.-Atmos., 110, D08106, doi:10.1029/2004JD005506, 2005.

Jäger, H. and Deshler, T.: Lidar backscatter to extinction, mass and area conversions for stratospheric aerosols based on mid-latitude balloonborne size distribution measurements, Geophys.Res. Lett., 29, 1929, doi:10.1029/2002GL015609, 2002.

Jäger, H., and Deshler, T.: Correction to Lidar backscatter to extinction, mass and area conversions for stratospheric aerosols based on midlatitude balloonborne size distribution measurements, Geophys. Res. Lett., 30, 7, 1382, doi: 10.1029/2003GL017189, 2003.

Jäger, H., and Hofmann, D. J.: Midlatitude lidar backscatter to mass, area and extinction conversion model based on in situ aerosol measurements from 1980 to 1987, Appl. Opt., 30, 127–138, https://doi.org/10.1364/AO.30.000127, 1991.

Jäger, H., Deshler, T., and Hofmann, D. J.: Midlatitude lidar backscatter conversions based on balloonborne aerosol measurements, Geophys. Res. Lett., 22, 1729–1732, https://doi.org/10.1029/95GL01521, 1995.

Jones, M. W., Smith, A., Betts, R., Canadell, J. G., Colin Prentice, I., and Le Quéré, C.: Climate Change Increases the Risk of Wildfires, ScienceBrief, https://sciencebrief.org/topics/climate-change-science/wildfires, 2020.

Kablick, G. P., Allen, D. R., Fromm, M. D., and Nedoluha, G. E.: Australian pyroCb smoke generates synoptic-scale stratospheric anticyclones. Geophysical Research Letters, 47, e2020GL088101, https://doi.org/10.1029/2020GL088101, 2020.

Kahnert, M.: Optical properties of black carbon aerosols encapsulated in a shell of sulfate: comparison of the closed cell modell with a coated aggregate model, Opt. Express, 25, doi:10.1364/OE.25.024579, 2017.

https://doi.org/10.5194/acp-2020-1093
Preprint. Discussion started: 23 November 2020

Atmospheric Chemistry and Physics Discussions

Kanji, Z. A., Welti, A., Corbin, J. C., and Mensah, A. A.: Black carbon particles do not matter for immersion mode ice nucleation. Geophysical Research Letters, 46, e2019GL086764. https://doi.org/10.1029/2019GL086764, 2020.

Kar, J., Lee, K.-P., Vaughan, M. A., Tackett, J. L., Trepte, C. R., Winker, D. M., Lucker, P. L., and Getzewich, B. J.: CALIPSO level 3 stratospheric aerosol profile product: version 1.00 algorithm description and initial assessment, Atmos. Meas. Tech., 12, 6173–6191, https://doi.org/10.5194/amt-12-6173-2019, 2019.

Khaykin, S., Legras, B., Bucci, S., Sellitto, P., Isaksen, L., Tencé, F., Bekki, S., Bourassa, A., Rieger, L., Tawada, D., Jumelet, J., and Godin-Beekmann, S.: The 2019/20 Australian wildfires generated a persistent smoke-charged vortex rising up to 35 km altitude, Commun Earth Environ, 1, 22, https://doi.org/10.1038/s43247-020-00022-5, 2020.

Kitzberger, T., Falk, D. A., Swetnam, T. W., and Westerling, L.: Heterogeneous responses of wildfire annual area burned to climate change across western and boreal North America, PLOS One, 12, e0188486. doi:https://doi.org/10.1371/journal.pone.0188486, 2017.

Knopf, D. A. and Alpert, P. A.: A water activity based modelof heterogeneous ice nucleation kinetics for freezing of waterand aqueous solution droplets, Farad. Discuss., 165, 513–534, doi:10.1039/c3fd00035d, 2013.

Knopf, D. A., Alpert, P. A., and Wang, B.:, The role of organic aerosol in atmospheric ice nucleation: a review, ACS Earth and Space Chemistry, 2, 168–202, https://doi.org/10.1021/acsearthspacechem.7b00120, 2018.

Koop, T., and Zobrist, B.: Parameterizations for ice nucleation in biological and atmospheric system, Phys. Chem. Chem. Phys., 11, 10839–10850, http://dx.doi.org/10.1039/B914289D, 2009.

Koop, T., Luo, B. P., Tsias, A., and Peter, T.: Water activity as the determinant for homogeneous ice nucleation in aqueous solutions, Nature, 406, 611–614, doi:10.1038/35020537, 2000.

Koop, T., Bookhold, J., Shiraiwa, M., and Pöschl, U.: Glass transition and phase state of organic compounds: dependency on molecular properties and implications for secondary organic aerosols in the atmosphere, Phys. Chem. Chem. Phys., 13, 19238–19255, http://dx.doi.org/10.1039/c1cp22617g, 2011.

Li, C., Hu, Y., Chen, J., Zhen, M., Ye, X., Yang, X., Wang, L., Wang, X., and Mellouki, A.: Physiochemical properties of carbonaceous aerosol from agricultural residue burning: density, volatility, and hygroscopicity, Atmos. Env., 140, 94–105, https://doi.org/10.1016/j.atmosenv.2016.05.052, 2016.

Liu, L., and Mishchenko, M. I.: Scattering and radiative properties of morphologically complex carbonaceous aerosols: A systematic modeling study. Remote Sens., 10, https://doi:10.3390/rs10101634, 2018.

Liu, L., and Mishchenko, M. I.: Spectrally dependent linear depolarization and lidar ratios for nonspherical smoke aerosols, J. Quant. Spec. Radiat. Trans., 248, https://doi.org/10.1016/j.jqsrt.2020.106953, 2020.

Liu, Y., Stanturf, J.A., and Goodrick, S.L.: Trends in global wildfire potential in a changing climate, For. Ecol. Manage., 259, 685–697, doi:10.1016/j.foreco.2009.09.002, 2009.

Liu, Y., Goodrick, S., and Heilman, W.: Wildland fire emissions, carbon, and climate: Wildfire-climate interactions, For. Ecol. Manage., 317, 80–96, http://dx.doi.org/10.1016/j.foreco.2013.02.020, 2014.

Mamali, D., Marinou, E., Sciare, J., Pikridas, M., Kokkalis, P., Kottas, M., Binietoglou, I., Tsekeri, A., Keleshis, C., Engelmann, R., Baars, H., Ansmann, A., Amiridis, V., Russchenberg, H., and Biskos, G.: Vertical profiles of aerosol mass concentration derived by unmanned airborne in situ and remote sensing instruments during dust events, Atmos. Meas. Tech., 11, 2897-2910, https://doi.org/10.5194/amt-11-2897-2018, 2018.

Mamouri, R. E. and Ansmann, A.: Estimated desert-dust ice nuclei profiles from polarization lidar: methodology and case studies, Atmos. Chem. Phys., 15, 3463-3477, doi:10.5194/acp-15-3463-2015, 2015.

https://doi.org/10.5194/acp-2020-1093
Preprint. Discussion started: 23 November 2020

Mamouri, R.-E. and Ansmann, A.: Potential of polarization lidar to provide profiles of CCN- and INP-relevant aerosol parameters, Atmos. Chem. Phys., 16, 5905-5931, doi:10.5194/acp-16-5905-2016, 2016.

Mamouri, R.-E. and Ansmann, A.: Potential of polarization/Raman lidar to separate fine dust, coarse dust, maritime, and anthropogenic aerosol profiles, Atmos. Meas. Tech., 10, 3403-3427, https://doi.org/10.5194/amt-10-3403-2017, 2017.

Marcolli, C.: Deposition nucleation viewed as homogeneous or immersion freezing in pores and cavities, Atmos. Chem. Phys., 14, 2071–2104, https://doi.org/10.5194/acp-14-2071-2014, 2014.

Marinou, E., Tesche, M., Nenes, A., Ansmann, A., Schrod, J., Mamali, D., Tsekeri, A., Pikridas, M., Baars, H., Engelmann, R., Voudouri, K.-A., Solomos, S., Sciare, J., Groß, S., Ewald, F., and Amiridis, V.: Retrieval of ice-nucleating particle concentrations from lidar observations and comparison with UAV in situ measurements, Atmos. Chem. Phys., 19, 11315–11342, https://doi.org/10.5194/acp-19-11315-2019, 2019.

Mattis, I., Seifert, P., Müller, D., Tesche, M., Hiebsch, A., Kanitz, T., Schmidt, J., Finger, F., Wandinger, U., and Ansmann, A.: Volcanic aerosol layers observed with multiwavelength Raman lidar over central Europe in 2008–-2009, J. Geophys. Res., 115, D00L04, doi:10.1029/2009JD013472, 2010.

Mayol-Bracero, O. L., Guyon, P., Graham, B., Roberts, G., Andreae, M. O., Decesari, S., Facchini, M. C., Fuzzi, S., and Artaxo, P.: Water-soluble organic compounds in biomass burning aerosols over Amazonia, 2. apportionment of the chemical composition and importance of the polyacidic fraction, J. Geophys. Res., 107, 8091–8106, doi:10.1029/2001JD000522, 2002.

Mikhailov, E., Vlasenko, S., Martin, S. T., Koop, T., and Pöschl, U.: Amorphous and crystalline aerosol particles interacting with water vapor: conceptual framework and experimental evidence for restructuring, phase transitions and kinetic limitations, Atmos. Chem. Phys., 9, 9491–9522, https://doi.org/10.5194/acp-9-9491-2009, 2009.

Möhler, O., Linke, C., Saathoff, H., Schnaiter, M., Wagner, R., Mangold, A., Krämer, M., and Schurath, U.: Ice nucleation on flame soot aerosol of different organic carbon content, Meteorol. Z., 48, 477–484, doi: 10.1127/0941-2948/2005/0055, 2005.

Müller, D., Wandinger, U., and Ansmann, A.: Microphysical particle parameters from extinction and backscatter lidar data by inversion with regularization: Theory, Appl. Opt., 38, 2346–2357, 1999.

Müller, D., Mattis, I., Wandinger, U., Ansmann, A., Althausen, A., and Stohl, A.: Raman lidar observations of aged Siberian and Canadian forest fire smoke in the free troposphere over Germany in 2003: Microphysical particle characterization, J. Geophys. Res., 110, D17201, doi:10.1029/2004JD005756, 2005.

Müller, D., Mattis, I., Ansmann, A., Wandinger, U., Ritter, C., and Kaiser, D.: Multiwavelength Raman lidar observations of particle growth during long-range transport of forest-fire smoke in the free troposphere, Geophys. Res. Lett., 34, L05803, doi:10.1029/2006GL027936, 2007.

Müller, D., Ansmann, A., Mattis, I., Tesche, M., Wandinger, U., Althausen, D., and Pisani, G.: Aerosol-type-dependent lidar ratios observed with Raman lidar, J. Geophys. Res., 112, D16202, doi:10.1029/2006JD008292, 2007b.

Müller, D., Hostetler, C. A., Ferrare, R. A., Burton, S. P., Chemyakin, E., Kolgotin, A., Hair, J. W., Cook, A. L., Harper, D. B., Rogers, R. R., Hare, R. W., Cleckner, C. S., Obland, M. D., Tomlinson, J., Berg, L. K., and Schmid, B.: Airborne Multiwavelength High Spectral Resolution Lidar (HSRL-2) observations during TCAP 2012: vertical profiles of optical and microphysical properties of a smoke/urban haze plume over the northeastern coast of the US, Atmos. Meas. Tech., 7, 3487–3496, https://doi.org/10.5194/amt-7-3487-2014, 2014

Murayama, T., Müller, D., Wada, K., Shimizu, A., Sekiguchi, M., and Tsukamoto, T.: Characterization of Asian dust and Siberian smoke with multi-wavelength Raman lidar over Tokyo, Japan in spring 2003, Geophys. Res. Lett., 31, L23103, doi:10.1029/2004GL021105, 2004.

https://doi.org/10.5194/acp-2020-1093
Preprint. Discussion started: 23 November 2020

Atmospheric Chemistry and Physics Discussions

Nicolae, D., Nemuc, A., Müller, D., Talianu, C., Vasilescu, J., Belegante, L., and Kolgotin, A.: Characterization of fresh and aged biomass burning events using multiwavelength Raman lidar and mass spectrometry, J. Geophys. Res. Atmos., 118, 2956–2965, doi:10.1002/jgrd.50324, 2013.

Nisantzi, A., Mamouri, R. E., Ansmann, A., and Hadjimitsis, D.: Injection of mineral dust into the free troposphere during fire events observed with polarization lidar at Limassol, Cyprus, Atmos. Chem. Phys., 14, 12155–12165, doi:10.5194/acp-14-12155-2014, 2014.

Noh, Y. M., Müller, D., Shin, D. H., Lee, H., Jung, J. S., Lee, K. H., Cribb, M., Li, Z., and Kim, Y. J.: Optical and microphysical properties of severe haze and smoke aerosol measured by integrated remote sensing techniques in Gwangju, Korea, Atmos. Environ., 43, 879–888, https://doi.org/10.1016/j.atmosenv.2008.10.058, 2009.

Omar, A. H., Winker, D. M., Kittaka, C., Vaughan, M. A., Liu, Z., Hu, Y., Trepte, C. R., Rogers, R. R., Ferrare, R. A., Lee, K.-P., Kuehn, R. E., and Hostetler, C. A.: The CALIPSO Automated Aerosol Classification and Lidar Ratio Selection Algorithm, J. Atmos. Ocean. Tech., 26, 1994–2014, https://doi.org/10.1175/2009JTECHA1231.1, 2009.

Ohneiser, K., Ansmann, A., Baars, H., Seifert, P., Barja, B., Jimenez, C., Radenz, M., Teisseire, A., Floutsi, A., Haarig, M., Foth, A., Chudnovsky, A., Engelmann, R., Zamorano, F., Bühl, J., and Wandinger, U.: Smoke of extreme Australian bushfires observed in the stratosphere over Punta Arenas, Chile, in January 2020: optical thickness, lidar ratios, and depolarization ratios at 355 and 532 nm, Atmos. Chem. Phys., 20, 8003–8015, https://doi.org/10.5194/acp-20-8003-2020, 2020.

PollyNet: PollyNET lidar data base, available at: http://polly.rsd.tropos.de/, last access: 20 August, 2020.

Reid, J. S., and Hobbs, P. V.: Physical and optical properties of young smoke from individual biomass fires in Brazil, J. Geophys. Res., 103, 32013-32030, doi:10.1029/98JD00159, 1998.

Reitebuch, O.: The Spaceborne Wind Lidar Mission ADM-Aeolus, in: Atmospheric Physics, Research Topics in Aerospace, edited by: Schumann, U., ISBN 978-3-642-30182-7, Springer-Verlag Berlin Heidelberg, 815–827, doi:10.1007/978-3-642-30183-4_49, 2012.

Reitebuch, O., Lemmerz, C., Lux, O., Marksteiner, U., Rahm, S.,Weiler, F., Witschas, B., Meringer, M., Schmidt, K., Huber, D., Nikolaus, I., Geiss, A., Vaughan, M., Dabas, A., Flament, T., Stieglitz, H., Isaksen, L., Rennie, M., de Kloe, J., Marseille, G.-J., Stoffelen, A., Wernham, D., Kanitz, T., Straume, A.-G., Fehr, T., von Bismark, J., Floberghagen, R., and Parrinello, T.: Initial assessment of the performance of the first wind lidar in space on Aeolus, EPJ Web of Conferences, Volume 237, 01010, The 29th International Laser Radar Conference (ILRC 29), 24–28 June 2019, Hefei, Anhui, China, https://doi.org/10.1051/epjconf/202023701010, 2020.

Rigg, Y. J., Alpert, P. A., and Knopf, D. A.: Immersion freezing of water and aqueous ammonium sulfate droplets initiated by humic-like substances as a function of water activity, Atmos. Chem. Phys., 13, 6603–6622, https://doi.org/10.5194/acp-13-6603-2013, 2013.

Sakai, T., Uchino, O., Nagai, T., Liley, B., Morino, I., and Fujimoto, T.: Long-term variation of stratospheric aerosols observed with lidars over Tsukuba, Japan, from 1982 and Lauder, New Zealand, from 1992 to 2015, J. Geophys. Res. Atmos., 121, 10283-10293, doi:10.1002/2016JD025132, 2016.

Schmidl, C., Bauer, H., Dattler, A., Hitzenberger, R., Weissenboeck, G., Marr, I. L., and Puxbaum, H.: Chemical characterisation of particle emissions from burning leaves, Atmos. Environ., 42, 9070–9079, doi:10.1016/j.atmosenv.2008.09.010, 2008a.

Schmidl, C., Marr, L. L., Caseiro, A., Kotianova, P., Berner, A., Bauer, H., Kasper-Giebl, A., and Puxbaum, H.: Chemical characterisation of fine particle emissions from wood stove combustion of common woods growing in mid- European Alpine regions, Atmos. Environ., 42, 126–141, doi:10.1016/j.atmosenv.2007.09.028, 2008b.

Schill, G. P., DeMott, P. J., Emerson, E. W., Rauker, A. M. C., Kodros, J. K., Suski, K. J., Hill, T. C. J., Levin, E. J. T., Pierce, J. R., Farmer, D. K., and Kreidenweis, S. M.: The contribution of black carbon to global ice nucleating particle concentrations relevant to mixed-phase clouds, Proceedings of the National Academy of Sciences, 117, 22705-22711, https://doi.org/10.1073/pnas.2001674117, 2020.

https://doi.org/10.5194/acp-2020-1093
Preprint. Discussion started: 23 November 2020

Atmospheric Chemistry and Physics Discussions

Shinozuka, Y., Clarke, A. D., Nenes, A., Jefferson, A., Wood, R., McNaughton, C. S., Ström, J., Tunved, P., Redemann, J., Thornhill, K. L., Moore, R. H., Lathem, T. L., Lin, J. J., and Yoon, Y. J.: The relationship between cloud condensation nuclei (CCN) concentration and light extinction of dried particles: indications of underlying aerosol processes and implications for satellite-based CCN estimates, Atmos. Chem. Phys., 15, 7585-7604, doi:10.5194/acp-15-7585-2015, 2015.

Shiraiwa, M., Li, Y., Tsimpidi, A., Karydis, V. A., Berkemeier, T., Pandis, S. N., Lelieveld, J., Koop, T., and Pöschl, U.: Global distribution of particle phase state in atmospheric secondary organic aerosols, Nature Communication, 8, 15002, https://doi.org/10.1038/ncomms15002, 2017.

Slade, J. H., Shiraiwa, M., Arangio, A., Su, H., Pöschl, U., Wang, J., and Knopf, D. A.: Cloud droplet activation through oxidation of organic aerosol influenced by temperature and particle phase state, Geophys. Res. Lett., 44, 1583– 1591, doi:10.1002/2016GL072424, 2017.

Taha, G., Loughman, R., Zhu, T., Thomason, L., Kar, J., Rieger, L., and Bourassa, A.: OMPS LP Version 2.0 Multi-wavelength Aerosol Extinction Coefficient Retrieval Algorithm, Atmos. Meas. Tech. Discuss., https://doi.org/10.5194/amt-2020-329, in review, 2020.

Tesche, M., Ansmann, A., Müller, D., Althausen, D., Engelmann, R., Freudenthaler, V., and Groß, S.: Vertically resolved separation of dust and smoke over Cape Verde using multiwavelength Raman and polarization lidars during Saharan Mineral Dust Experiment 2008, J. Geophys. Res., 114, D13202, doi:10.1029/2009JD011862, 2009.

Tesche, M., Müller, D., Groß, S., Ansmann, A., Althausen, D., Freudenthaler, V., Weinzierl, B., Veira, A., and Petzold, A.: Optical and microphysical properties of smoke over Cape Verde inferred from multiwavelength lidar measurements. Tellus B, 63, 677–694, doi:10.1111/j.1600-0889.2011.00549.x, 2011.

Torres, O., Bhartia, P. K., Taha, G., Jethva, H., Das, S., Colarco, P., Krotkov, N., Omar, A., and Ahn, C.: Stratospheric Injection of Massive Smoke Plume from Canadian Boreal Fires in 2017 as seen by DSCOVR-EPIC, CALIOP and OMPS-LP Observations. Journal of Geophysical Research: Atmospheres, 125, e2020JD032579, https://doi.org/10.1029/2020JD032579, 2020.

Trickl, T., Giehl, H., Jäger, H., and Vogelmann, H.: 35 yr of stratospheric aerosol measurements at Garmisch-Partenkirchen: from Fuego to Eyjafjallajökull, and beyond, Atmos. Chem. Phys., 13, 5205-5225, https://doi.org/10.5194/acp-13-5205-2013, 2013.

Ullrich, R., Hoose, C., Möhler, O., Niemand, M., Wagner, R., Höhler, K., Hiranuma, N., Saathoff, H., and Leisner, T.: A new ice nucleation active site parameterization for desert dust and soot, J. Atmos. Sci., 74, 699–717, doi: 10.1175/JAS-D-16-0074.1, 2017.

Veselovskii I., Kolgotin, A., Griaznov, V., Müller, D., Wandinger, U., and Whiteman, D.: Inversion with regularization for the retrieval of tropospheric aerosol parameters from multi-wavelength lidar sounding, Appl. Opt., 41, 3685–3699, https://doi.org/10.1364/AO.41.003685, 2002.

Veselovskii, I., Dubovik, O., Kolgotin, A., Korenskiy, M., Whiteman, D. N., Allakhverdiev, K., and Huseyinoglu, F.: Linear estimation of particle bulk parameters from multi-wavelength lidar measurements, Atmos. Meas. Tech., 5, 1135–1145, doi:10.5194/amt-5-1135-2012, 2012.

Veselovskii, I., Whiteman, D. N., Korenskiy, M., Suvorina, A., Kolgotin, A., Lyapustin, A., Wang, Y., Chin, M., Bian, H., Kucsera, T. L., Pérez-Ramírez, D., and Holben, B.: Characterization of forest fire smoke event near Washington, DC in summer 2013 with multi-wavelength lidar, Atmos. Chem. Phys., 15, 1647-1660, https://doi.org/10.5194/acp-15-1647-2015, 2015.

Wagner, R., Jähn, M., and Schepanski, K.: Wildfires as a source of airborne mineral dust – revisiting a conceptual model using large-eddy simulation (LES), Atmos. Chem. Phys., 18, 11863–11884, https://doi.org/10.5194/acp-18-11863-2018, 2018.

Wandinger, U., Müller, D., Böckmann, C., Althausen, D., Matthias, V., Bösenberg, J, Weiß, V., Fiebig, M., Wendisch, M., Stohl, A., and Ansmann. A.: Optical and microphysical characterization of biomass-burning and industrial-pollution aerosols from multiwavelength lidar and aircraft measurements, J. Geophys. Res.,107(D21), doi:10.1029/2000JD000202,2002.

https://doi.org/10.5194/acp-2020-1093
Preprint. Discussion started: 23 November 2020

Wang, B., and Knopf, D. A.: Heterogeneous ice nucleation on particles composed of humic-like substances impacted by O_3, J. Geophys. Res., 116, D03205, doi:10.1029/2010JD014964, 2011.

Wang, B., Lambe, A. T., Massoli, P., Onasch, T. B., Davidovits, P., Worsnop, D. R., and Knopf, D. A.: The deposition ice nucleation and immersion freezing potential of amorphous secondary organic aerosol: Pathways for ice and mixed-phase cloud formation, J. Geophys. Res., 117, D16209, doi:10.1029/2012JD018063, 2012.

Winker, D. M., Vaughan, M. A., Omar, A., Hu, Y., Powell, K. A., Liu, Z., Hunt, W. H., and Young, S. A.: Overview of the CALIPSO mission and CALIOP data processing algorithms, J. Atmos. Oceanic Technol., 26, 2310–2323, https://doi.org/10.1175/2009JTECHA1281.1, 2009.

Yu, P., Toon, O. B., Bardeen, C. G., Zhu, Y., Rosenlof, K. H., Portmann, R. W., Thornberry, T. D., Gao, R.-S., Davis, S. M., Wolf, E. T., de Gouw, J., Peterson, D. A., Fromm, M. D., and Robock, A.: Black carbon lofts wildfire smoke high into the stratosphere to form a persistent plume, Science, 365, 587–590, doi: 10.1126/science.aax1748, 2019.

Zobrist, B., Marcolli, C., Pedernera, D. A., and Koop, T.: Do atmospheric aerosols form glasses?, Atmos. Chem. Phys., 8, 5221–5244, https://doi.org/10.5194/acp-8-5221-2008, 2008.

Zuev, V. V., Gerasimov, V. V., Nevzorov, A. V., and Savelieva, E. S.: Lidar observations of pyrocumulonimbus smoke plumes in the UTLS over Tomsk (Western Siberia, Russia) from 2000 to 2017, Atmos. Chem. Phys., 19, 3341-3356, https://doi.org/10.5194/acp-19-3341-2019, 2019.

https://doi.org/10.5194/acp-2020-1093
Preprint. Discussion started: 23 November 2020

Atmospheric Chemistry and Physics Discussions

Table 1. Overview of the step-by-step computations to obtain smoke microphyscal properties $v(z)$, $M(z)$, $s(z)$, $n_{50}(z)$, and $n_{250}(z)$ as well as estimates of cloud relevant parameters $n_{\mathrm{CCN}}(z)$ for a water supersaturation $S_{\mathrm{w}} = 0.2\%$ and $n_{\mathrm{INP}}(z)$ from the smoke-related particle backscatter coefficient $\beta(z)$. The required conversion factors c_{v}, c_{s}, c_{100}, and c_{250} are listed in Table 4. An appropriate smoke lidar ratio S_{L} is needed in step 2 to convert the smoke backscatter profiles, $\beta(z)$ into extinction coefficients $\sigma(z)$. Besides the surface area values, $s(z)$, the temperature ($T(z)$) and relative humidity information ($RH_{\mathrm{i}}, S_{\mathrm{i}}$) is needed in the estimation of ice-nucleating particle concentrations $n_{\mathrm{INP}}(z)$. KA13 (wildfire smoke, immersion freezing) (Knopf and Alpert, 2013) and WK11 (wildfire smoke, deposition nucleation) (Wang and Knopf, 2011) INP parameterization schemes are applied. r denotes the radius of the particles. Uncertainties (right column) are discussed in Mamouri and Ansmann (2016, 2017) and represent typical uncertainties caused by the errors in the forgoing retrieval steps and required input parameters. See text in Sect. 3.2 for more details.

Step	Smoke parameter	Product/computation	Uncertainty
1	Backscatter coefficient [$\mathrm{Mm^{-1}\ sr^{-1}}$]	$\beta(z)$	10–20%
2	Extinction coefficient [$\mathrm{Mm^{-1}}$]	$\sigma(z)$=$S_{\mathrm{L}}\beta(z)$	20–30%
3	Volume concentration [$\mathrm{m^{-3}}$]	$v(z) = c_{\mathrm{v}}\sigma(z)$	25–35%
4	Mass concentration [$\mu\mathrm{g\ m^{-3}}$]	$M(z) = \rho c_{\mathrm{v}}\sigma(z)$	30–40%
5	Surface concentration [$\mathrm{m^2\ cm^{-3}}$]	$s(z) = c_{\mathrm{s}}\sigma(z)$	25–35%
6	Number concentration (r >50 nm) [$\mathrm{cm^{-3}}$]	$n_{50}(z) = c_{50}(\frac{\sigma(z)}{1\ \mathrm{Mm^{-1}}})^x$	50–200%
7	Number concentration (r >250 nm) [$\mathrm{cm^{-3}}$]	$n_{250}(z) = c_{250}\sigma(z)$	25–40%
8	CCN concentration [$\mathrm{cm^{-3}}$]	$n_{\mathrm{CCN}} \approx n_{50}(z)$	50–200%
9	INP concentration [$\mathrm{L^{-1}}$]	$n_{\mathrm{INP,I}}(z)$ (KA13), $n_{\mathrm{INP,D}}(z)$ (WK11)	-

https://doi.org/10.5194/acp-2020-1093
Preprint. Discussion started: 23 November 2020

Atmospheric Chemistry and Physics Discussions

Table 2. Selected smoke lidar ratios (S_{L}) for 355 nm and 532 nm to indicate the large range of possible values.

Atmospheric layer	$S_{\mathrm{L}}(355\ \mathrm{nm})$	$S_{\mathrm{L}}(532\ \mathrm{nm})$
Stratosphere, Canadian smoke:		
Haarig et al. (2018), aged	35–50 sr	50-80 sr
Stratosphere, Australian smoke:		
Ohneiser et al. (2020), aged	50-95 sr	70–110 sr
Troposphere, Canadian and Siberian smoke:		
Wandinger et al. (2002), aged	40–70 sr	40–80 sr
Murayama et al. (2004), aged	40 sr	65 sr
Veselovskii et al. (2015), fresh	65–90 sr	65–80 sr
Troposphere, European smoke:		
Alados-Arboledas et al. (2011), fresh	60–65 sr	60–65 sr
Nicolae et al. (2013), fresh, aged	30–60 sr	45-65 sr
Troposphere, Amazonian smoke:		
Baars et al. (2012), fresh	50–75 sr	50–80 sr
Troposphere, South African smoke:		
Giannakaki et al. (2015), fresh	70–110 sr	60–105 sr

Table 3. Values for b and m for three organic-aerosol INP types required to determine the ice nucleation rate $J_{\mathrm{het,I}}$ with Eq. (3).

INP type	b	m	Reference
Pahokee Peat (organic substance)	-15.78	78.31	Knopf and Alpert (2013)
Leonardite (organic substance)	-13.40	66.90	Knopf and Alpert (2013)
Free tropospheric aerosol (smoke plumes over Azores)	0.656	2.981	China et al. (2017)

https://doi.org/10.5194/acp-2020-1093
Preprint. Discussion started: 23 November 2020

Atmospheric Chemistry and Physics Discussions

Table 4. Smoke conversion parameters required in the conversion of particle extinction coefficients σ at 532 nm into particle number, surface area and volume concentration as described in Table 1. The mean values and SD for c_v, c_s, c_{250}, c_{50}, and x are obtained from the extended AERONET data analysis described in Sect. 4.2. Conversion factors are derived from the observations at Yellowknife (for fresh smoke) and Churchill (for weakly aged smoke) and from observations at Punta Arenas, CEILAP-RG, and Marambio (for aged smoke). Fresh (f), weakly aged (wa), and aged smoke denote smoke plumes 0.5–2.5 day, 2.5–5 days, and >5 days after emission. For the AERONET observations we provide mass-specific extinction coefficients $k_{ext} = 1/(\rho c_v)$ for the mean c_v values and the particle density range from 1.1–1.3 g cm^{-3}.

Observation (site)	c_v [10^{-12} Mm]	k_{ext} m^2 g^{-1}	c_s [10^{-12} Mm m^2 cm^{-3}]	c_{250} [Mm cm^{-3}]	c_{50} [cm^{-3}]	x
Aged smoke						
AERONET (Punta Arenas, CEILAP, Marambio)	0.137 ± 0.010	5.6-6.6	1.73 ± 0.28	0.37 ± 0.07	28.2 ± 14.5	0.71 ± 0.13
Lidar (Punta Arenas)	0.131 ± 0.008		1.41 ± 0.01	–	–	–
Lidar (Lindenberg)	0.141 ± 0.005		1.67 ± 0.29	–	–	–
Lidar (North Pole)	0.124 ± 0.006		1.78 ± 0.17	–	–	–
Fresh (f)and weakly aged (wa) smoke						
AERONET (Yellowknife, f)	0.192 ± 0.026	4.0–4.7	2.62 ± 0.35	0.17 ± 0.03	–	–
AERONET (Yellowknife, Churchill, f+wa)	0.181 ± 0.030	4.3–5.0	2.38 ± 0.38	0.20 ± 0.04	77.3 ± 40.5	0.71 ± 0.10
AERONET (Churchill, wa)	0.169 ± 0.030	4.6–5.4	2.15 ± 0.26	0.22 ± 0.04	–	–
AERONET (Leipzig, Lindenberg, wa)	0.164 ± 0.009	4.4–5.5	1.88 ± 0.21	0.23 ± 0.04	–	–
Lidar (Washington)	0.153 ± 0.005		2.11 ± 0.10	–	–	–
Lidar (Amazonia)	0.207 ± 0.029		2.18 ± 0.26	–	–	–

https://doi.org/10.5194/acp-2020-1093
Preprint. Discussion started: 23 November 2020

Atmospheric Chemistry and Physics Discussions

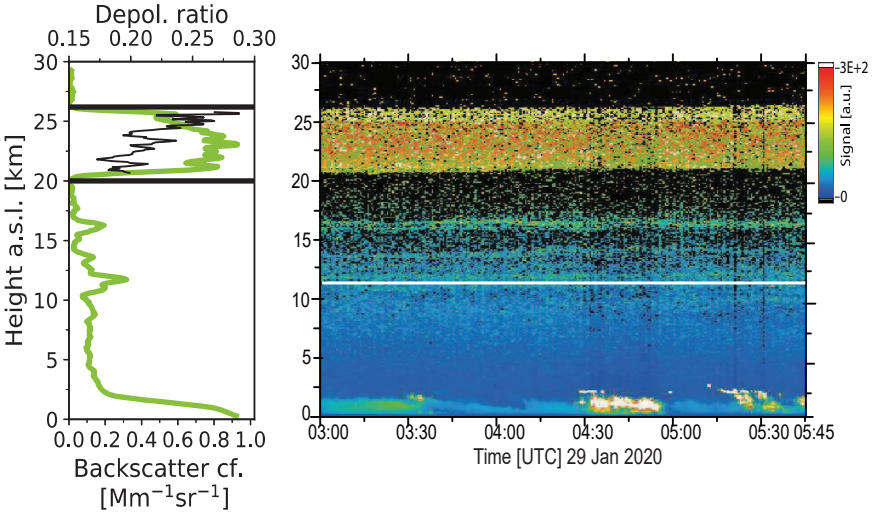

Figure 1. Australian bushfire smoke in the stratosphere above the tropopause (white line in the right panel). The mean backscatter coefficient profile (green) and the particle depolarization ratio (black, for the main layer only) are shown in the left panel. Main smoke layer base and top height are indicated by black horizontal lines. The smoke was observed with lidar at Punta Arenas, Chile, on 29 January 2020, about 10000 km downwind of the Australian fire areas. The range-corrected 1064 nm lidar return signal is shown.

https://doi.org/10.5194/acp-2020-1093
Preprint. Discussion started: 23 November 2020

Atmospheric Chemistry and Physics Discussions

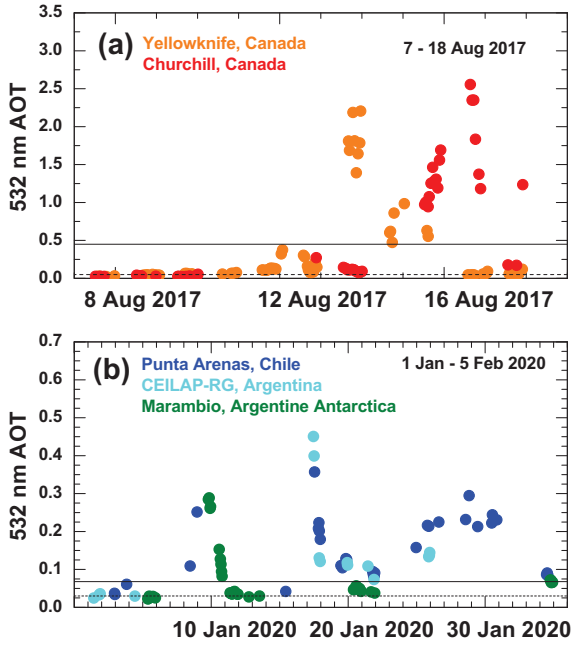

Figure 2. 532 nm AOT time series for different AERONET stations in (a) northern-central Canada (Yellowknife, 62.5°N, 114.4°W, and Churchill 58.7°N, 93.8°W) in the near range to major wild fires in western Canada and (b) in southern South America (CEILAP-RG, 51.6°S, 69.3°W and Punta Arenas, 53.1°S, 70.9°W) and in northern Antarctica (Marambio, 64.2°S, 56.6°W), about 10000 km east of the Australian wildfires sources. The dashed horizontal lines indicate the background AOT level, the solid lines the lower limit of AOT values considered in the determination of conversion parameters.

https://doi.org/10.5194/acp-2020-1093
Preprint. Discussion started: 23 November 2020

Atmospheric Chemistry and Physics Discussions

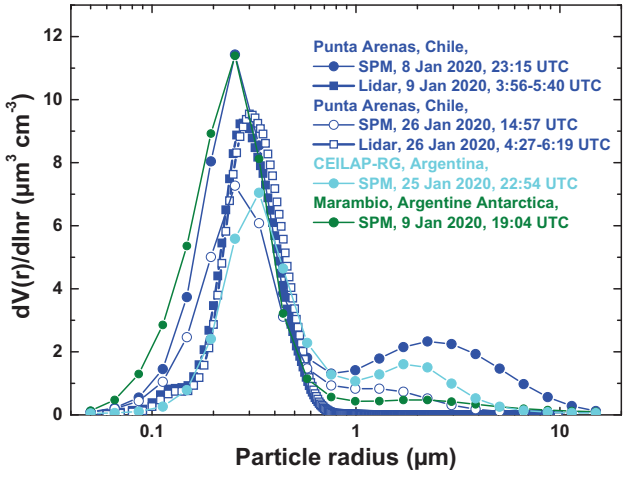

Figure 3. Particle volume size distribution derived from column (tropospheric + stratospheric) AERONET observations at Punta Arenas, the CEILAP-RG station, and Marambio in January 2020. In addition, size distributions for the well-identified stratospheric smoke layer are shown, obtained from the inversion of lidar-derived optical properties (squares). Two of the AERONET size distribution (CEILAP-RG, 25 January, Punta Arenas, 8 January) show a weak coarse mode (bimodal shape of the spectrum), the other size distribution a dominating accumulation mode (monomodal spectrum) in agreement with the lidar observations.

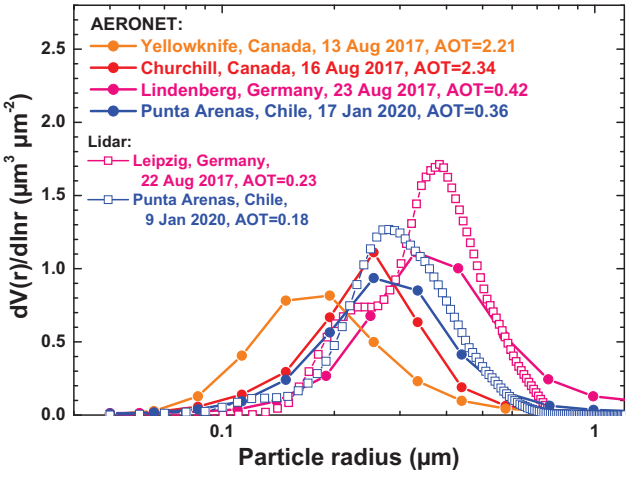

Figure 4. Comparison of different normalized particle volume size distributions highlighting the shift of the size distribution towards larger particles as a function of travel time. The Canadian smoke over Yellowknife (orange), Churchill (red), and Lindenberg (pink) was observed 1, 3-4, and 10-11 days after injection of smoke into the UTLS regime. The Punta Arenas observation (blue) was taken after 10 days of long-range transport. The stratospheric size distributions obtained from lidar observations match well with the respective observations at Punta Arenas and Lindenberg, corroborating that the AERONET observations are dominated by AOT contributions from stratospheric smoke. The mode radius shifted from 150-200 nm (Yellowknife) to 300-400 nm (Lindenberg) within the 10-day travel period.

https://doi.org/10.5194/acp-2020-1093
Preprint. Discussion started: 23 November 2020

Atmospheric Chemistry and Physics Discussions

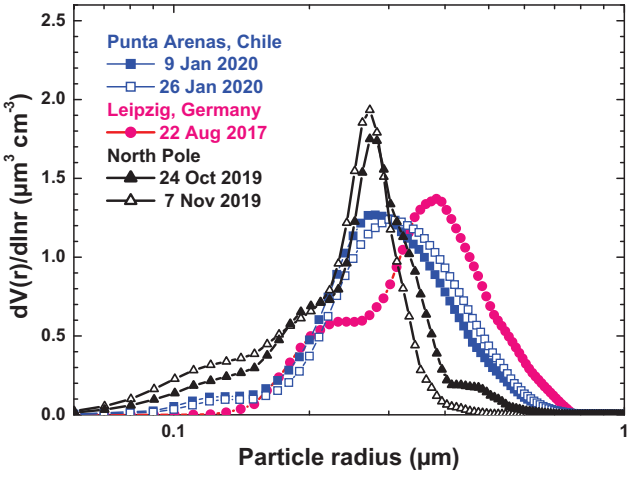

Figure 5. Lidar-derived normalized volume size distributions of stratospheric smoke particles found for Canadian smoke over Leipzig, Australian smoke over Punta Arenas, and Siberian and Alaskan smoke over the North Pole region.

https://doi.org/10.5194/acp-2020-1093
Preprint. Discussion started: 23 November 2020

Atmospheric Chemistry and Physics Discussions

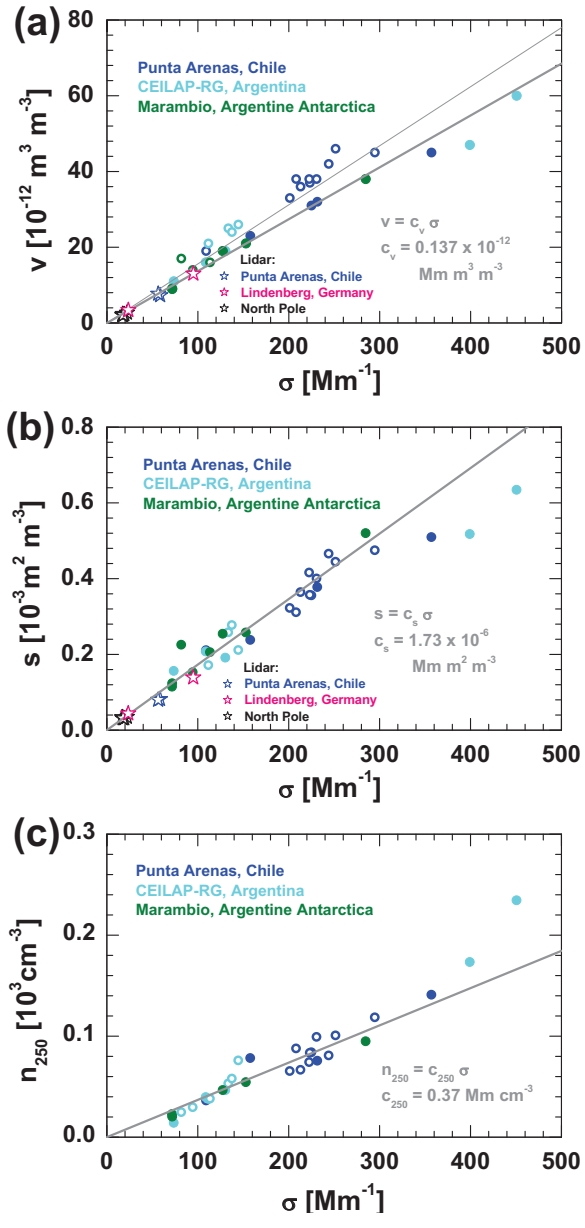

Figure 6. Relationship between dust extinction coefficient σ (532 nm) and (a) volume concentration v, (b) surface area concentration s, and (c) particle number concentration n_{250} for aged stratospheric Australian smoke observed over three AERONET stations. The slopes of the dark lines indicate the mean increase of v, s, and n_{250} with σ defined by equations given in the different panels. The conversion factors c_v (a, Eq. 12, for monomodal cases), c_s (b, Eq. 14), and c_{250} (c, Eq. 13) obtained from the correlations are also given as numbers. In (a), we distinguish between conversion factors (and straight lines) for cases with size distributions showing a monomodal shape (solid circles, thick line) and conversion factors considering all observations, i.e., by including the cases with bimodal shape (open symbols) of the particle size distribution (thin line). Such a separation was not carried out in (b) and (c). Also shown are several lidar observations (stars in a and b) of aged smoke layers in the free troposphere (Lindenberg) and in the UTLS region (Punta Arenas, North Pole) obtained by using the multiwavelength lidar inversion technique.

https://doi.org/10.5194/acp-2020-1093
Preprint. Discussion started: 23 November 2020

Atmospheric Chemistry and Physics Discussions

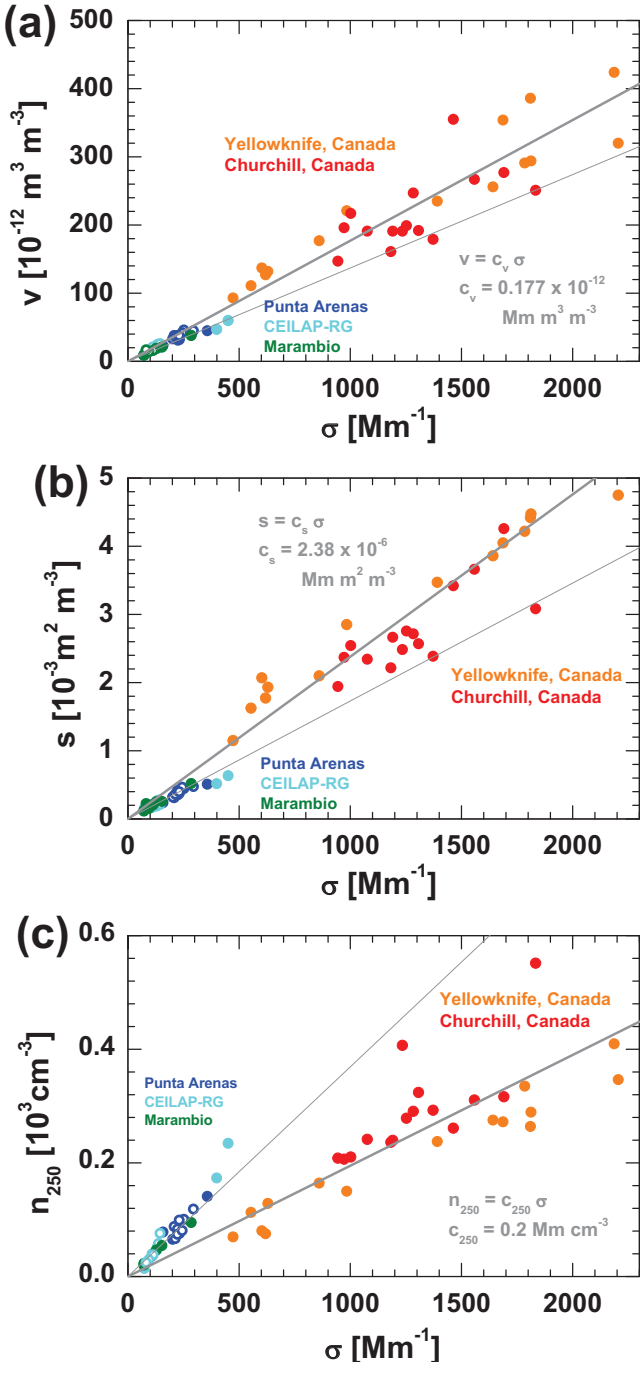

Figure 7. Same as Fig. 6 except for fresh and weakly aged stratospheric smoke observed over Yellowknife and Churchill in August 2017. For comparison southern hemispheric stratospheric aged smoke observations as given in Fig. 6 are added (blue and green colors, including thin straight lines representing the aged-smoke conversion factors).

https://doi.org/10.5194/acp-2020-1093
Preprint. Discussion started: 23 November 2020

Atmospheric Chemistry and Physics Discussions

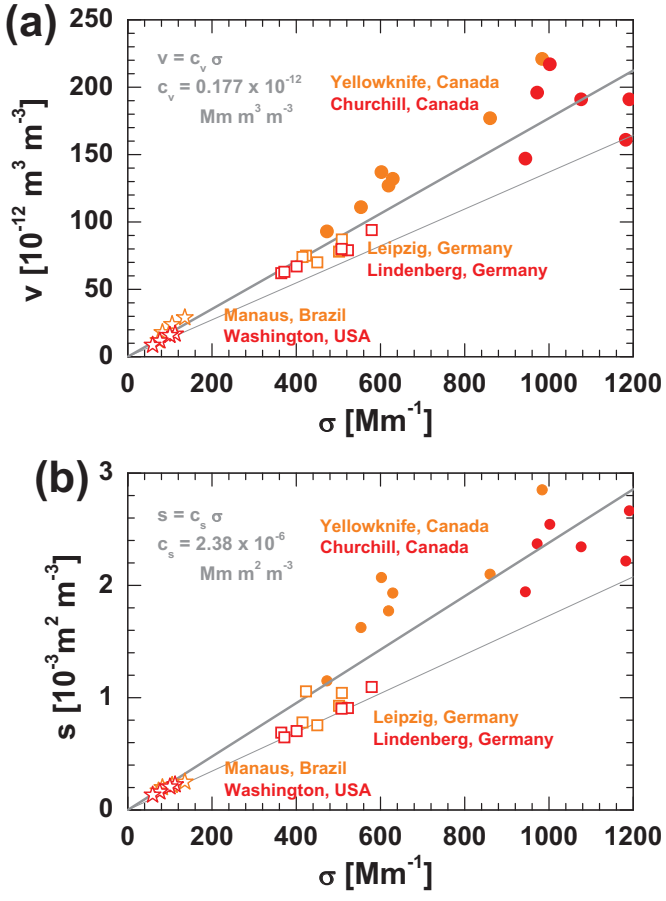

Figure 8. Same as Fig. 7 except for fresh and weakly aged smoke observations only. Besides the Yellowknife and Churchill AERONET observations in August 2017, several lidar observations performed in well-defined and identified layers of fresh and weakly aged smoke in the free troposphere (stars, Washington, USA, Manaus, Brazil) obtained from multiwavelength lidar inversion analysis are added. Recent tropospheric smoke observations performed at the AERONET sites of Leipzig and Lindenberg on 12 September 2020 (after three-day travel) are included as well (squares). Thick and thin straight lines are the same as in Fig. 7.

https://doi.org/10.5194/acp-2020-1093
Preprint. Discussion started: 23 November 2020

Atmospheric Chemistry and Physics Discussions

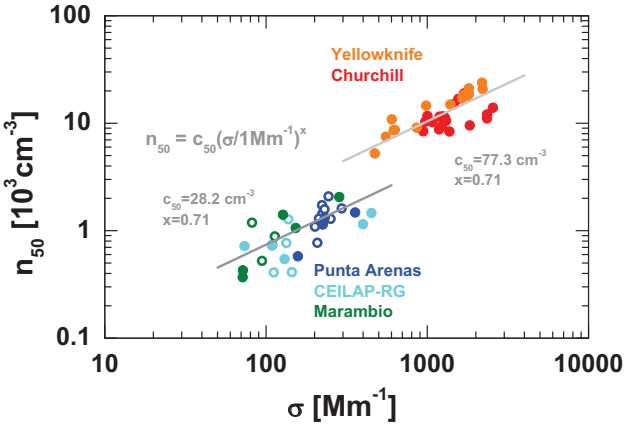

Figure 9. Relationship between smoke extinction coefficient σ (532 nm) and particle number concentration n_{50} for the different AERONET data sets (fresh smoke vs aged smoke). Clear differences for fresh and aged smoke are visible. More details in the text.

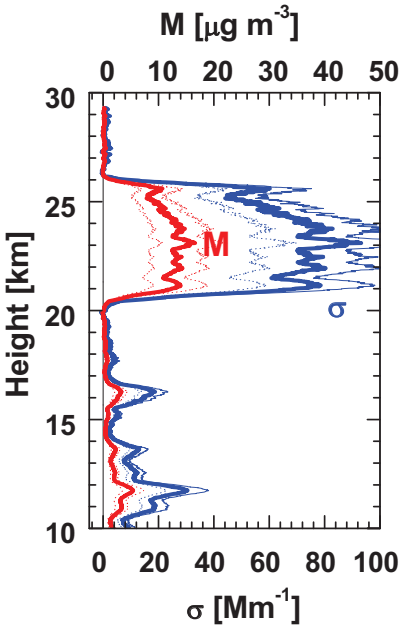

Figure 10. Smoke observation with lidar in the stratosphere over Punta Arenas on 29 January 2020 (see Fig. 1) in terms of particle extinction coefficient σ and particle mass concentration M. Extinction coefficients were obtained by multiplying the respective backcatter coefficients with a lidar ratio of 95 sr. Typical uncertainties of 25% and 35% in the extinction and mass retrievals, respectively, are shown as thin dotted lines.

https://doi.org/10.5194/acp-2020-1093
Preprint. Discussion started: 23 November 2020

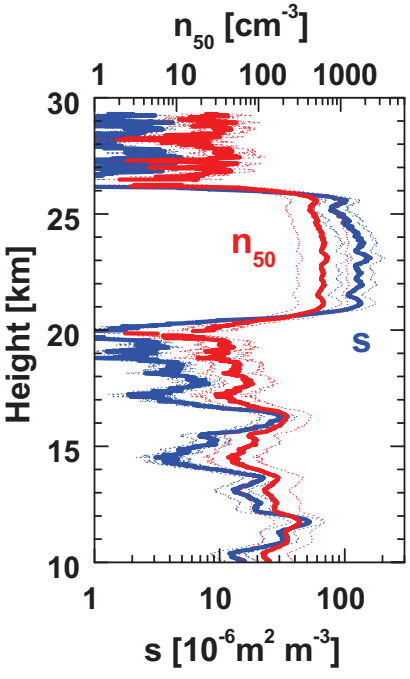

Figure 11. Retrieval results for 29 January 2020 in terms of surface area s and particle number concentration n_{50} (proxy for CCN) with error margins representing typical uncertainties (30% for s and a factor of 2 for n_{50}).

https://doi.org/10.5194/acp-2020-1093
Preprint. Discussion started: 23 November 2020

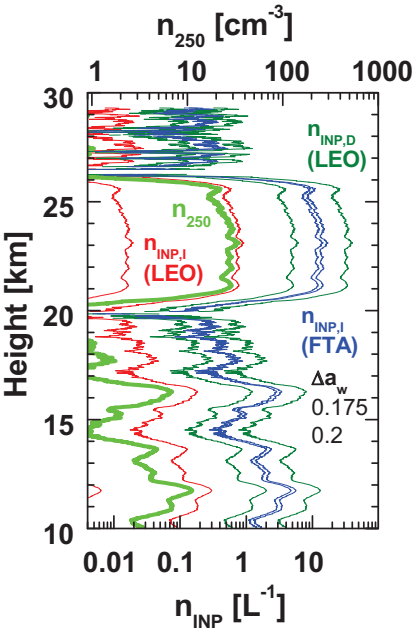

Figure 12. Retrieval results for 29 January 2020 in terms of INP concentrations $n_{\mathrm{INP,I}}$ and $n_{\mathrm{INP,D}}$ and large particle number concentration n_{250} (considering particles with radius >250 nm). See text for more details of the INP computations in the case of immersion freezing (blue and red profiles) and deposition nucleation (olive profiles). Different organic aerosol types (Leonardite, Leo, and a free tropospheric aerosol, FTA, with smoke signatures, Table 3) are considered. The INP concentrations are estimated by assuming an air parcel lifting period of 600 s (period of supersaturation expressed in Δa_{w} of 0.175 (low INP numbers) and 0.2 (high INP values)) and ice nucleation temperature of -50°C.

https://doi.org/10.5194/acp-2020-1093
Preprint. Discussion started: 23 November 2020

Atmospheric Chemistry and Physics Discussions

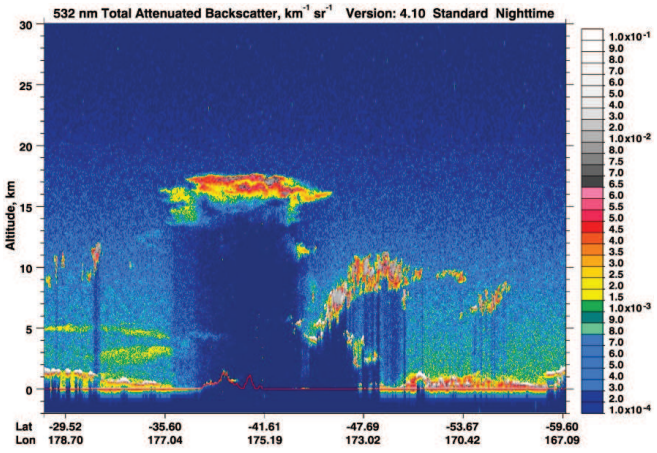

Figure 13. CALIPSO lidar observations of a stratospheric smoke layer between 13.5–17.5 km height over New Zealand (35–42°S) on 1 January 2020 around 13:00 UTC (CALIPSO, 2020a). The plume was injected during a strong and long-lasting pyro-Cb event on 30-31 December 2019 (Ohneiser et al., 2020) and then ascended by several kilometers within the next 24-36 hours.

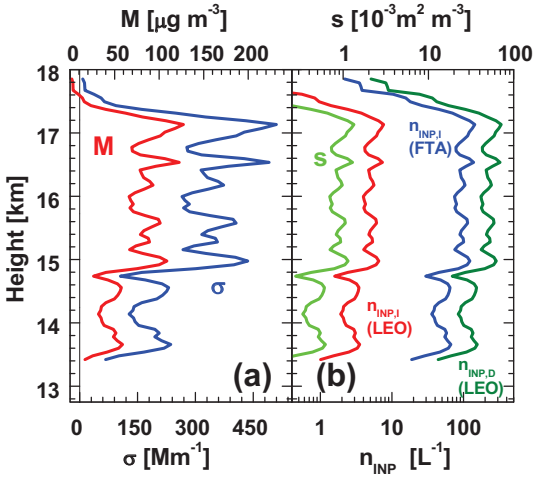

Figure 14. CALIPSO smoke observation in the stratosphere over New Zealand on 1 January 2020 in terms of (a) particle extinction coefficient σ, mass concentration M, and (b) INP concentration estimates $n_{\mathrm{INP,I}}$ and $n_{\mathrm{INP,D}}$ (for the same conditions as assumed in Fig. 12, $T = -50^{\circ}$C, $\Delta a_{\mathrm{w}} = 0.2$). The lidar-derived input parameter is the shown surface area concentration s. The CALIPSO backscatter coefficients were downloaded and averaged over the range from 35.3–40.5°S (horizontal range of 500 km) (CALIPSO, 2020b) and then multiplied with 95 sr to obtain the extinction coefficients. Error margins are not given in this figures. The uncertainties are of the order of 25% (σ), 35% (M), 30% (s), and 1-2 orders of magnitude (n_{INP}). The conversion factors for fresh smoke in Table 4 were applied. See text for more details of the computations of immersion freezing INP (red, blue) and deposition nucleation INP concentrations.

https://doi.org/10.5194/acp-2020-1093
Preprint. Discussion started: 23 November 2020

Atmospheric Chemistry and Physics Discussions

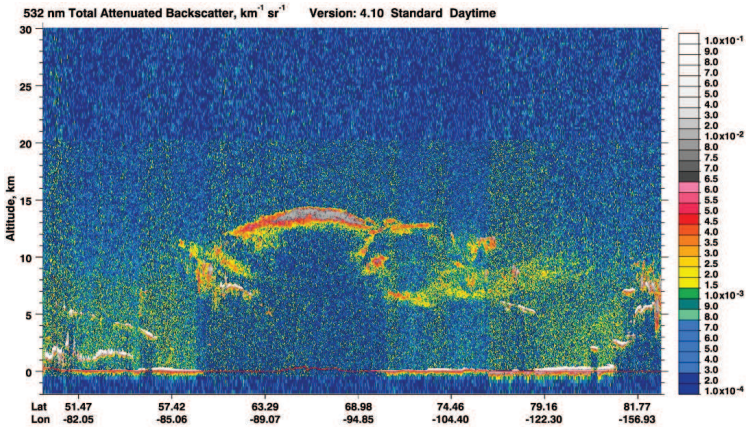

Figure 15. Same as Fig. 13, except for a smoke observation over the Hudson Bay, Canada, about 400-500 km east of the Churchill AERONET station on 15 August 2017, 18:30 UTC, about 66 hours after injection (CALIPSO, 2020a). The Churchill photometer measured AOTs from 1.2–1.6 at 500 nm in good agreement with the CALIPSO observation between 58-63°N. The smoke plume was injected during the strong and long-lasting pyro-Cb events on 12-13 August 2017.

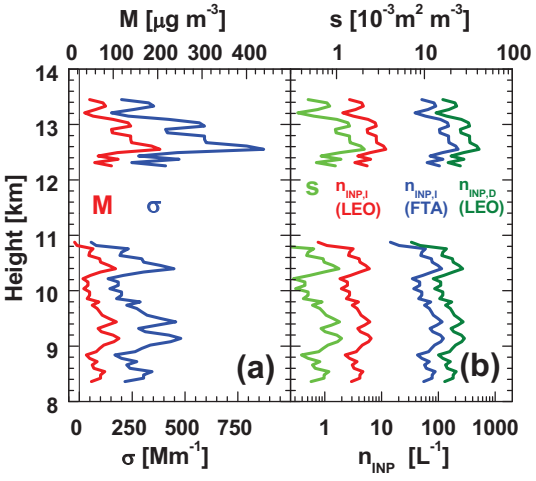

Figure 16. Same as Fig. 14, except for the smoke observation over the Hudson Bay, Canada, on 15 August 2017, 18:30 UTC. Two 100 km signal profile segments were selected and averaged (CALIPSO, 2020b). All data above 12 km were collected in the latitudinal range from 62.5-63.4°N (88.5-89.1°E), and all values below 11 km were collected in the latitudinal band from 58.2-59.0°N (85.5-86.1°E)). The downloaded and averaged backscatter coefficient profiles were multiplied with a smoke lidar ratio of 80 sr and then converted into mass and surface area concentrations by using the fresh-smoke conversion factors. The INP estimation is performed as in Fig. 12.